Depósito de Investigación de la Universidad de Sevilla

https://idus.us.es/

MWCNT/epoxy strip-like sensors for buckling detection in beam-like structures

Enrique García-Macías[a,*], Luis Rodríguez-Tembleque[a], Andrés Sáez[a]

[a]*Department of Continuum Mechanics and Structural Analysis, School of Engineering, Universidad de Sevilla, Spain*

Abstract

Buckling of slender structures constitutes a hazardous failure mechanism that can yield partial or total collapses. Nonetheless, given that buckling failure is characterized by a highly non-linear and sudden loss of stability, most off-the-shelf monitoring systems fail to detect buckling and very few research works in the literature can be found in this regard. Recent advances in the field of Nanotechnology have fostered the development of innovative composite materials with multifunctional properties, offering vast possibilities in the field of Structural Health Monitoring. Along these lines, the present work proposes a novel concept of smart beams for buckling detection applications. This consists of the deployment of carbon nanotube-reinforced epoxy strip-like sensors on the upper and bottom faces of a beam-like structure. Carbon nanotube-reinforced composites exhibit strain self-sensing capabilities, that is to say, these composites provide measurable variations in their electrical properties under the action of mechanical strains. In this way, the proposed sensing strips not only act as mechanical reinforcements, but also confer self-diagnostic properties to the system. The failure detection principle of the proposed smart beams consists of the assessment of the bending-induced variations of the normal strains during buckling. To do so, the electrical resistance of the sensing strips is continuously monitored through a two-probe resistivity measurement scheme. The present research furnishes detailed numerical parametric analyses to investigate the effectiveness of the proposed smart beams to detect buckling under uniaxially compression, as well as to evaluate the influence of design parameters such as filler volume fraction, boundary conditions and electrodes layouts. The macroscopic behaviour of the smart beams is simulated by a micromechanics-based piezoresistivity model and a multiphysics finite element code. The numerical results demonstrate that the buckling failure can be tracked through sudden disturbances in the electrical output of the smart strips.

Keywords: Carbon nanotube, Buckling detection, Self-sensing, Piezoresistivity, Smart material, Structural Health Monitoring

1. Introduction

Structural Health Monitoring (SHM) has become a consolidated discipline in many areas of Engineering and constitutes today a common practice in manifold industrial activities. This encompasses the application of Non-Destructive Testing (NDT) and damage detection in order to evaluate the soundness of infrastructures and conduct timely condition-based maintenance that allows expanding their life span [1]. In particular, most research efforts have focused on detecting damages through variations of the stiffness properties of structural members. Such variations often stem from aging degradation processes, corrosion, fatigue, cracking or accidental events [2]. Nevertheless, the number of studies on the application of SHM techniques to detect the loss of structural stability, that is buckling failure, are sorely lacking. Instability phenomena are highly determined by geometric and material non-linearities which limit the effectiveness of most off-the-shelf sensing solutions. The recent development of multifunctional composite materials, often termed smart materials, offers an innovative solution in the assessment of the integrity of structures. Particularly attractive are the self-sensing materials which fulfil a structural function and, at the same time, provide self-diagnostic capabilities apt for condition-based maintenance [3, 4]. While promising, the application of these novel materials is still at a very early stage and, indeed, their application for buckling detection is yet to be explored.

Even though instability is a fundamental strength limit state in design codes, few research works in the literature have reported about the application of monitoring systems for buckling detection. Among them, one approach is the Vibration Correlation Technique (VCT) which tracks the change in natural frequencies identified

---

*Corresponding author.
Email address:* `egarcia28@us.es` (Enrique García-Macías)

from acceleration records in order to estimate the buckling loads [5]. Both theoretical and experimental results have demonstrated that the natural frequencies of isolated structural members decrease for increasing compression loads and, in particular, the fundamental frequency decreases to zero when the load reaches the critical buckling load [6]. Therefore, buckling failure can be identified by continuous monitoring of the natural frequencies. Although these approaches have been shown effective for the buckling detection of isolated structural members like beams [7] or panels [8], their application to full-scale structures is limited, since the local buckling of a member is often hardly noticeable in the global natural frequencies. Qu *et al.* [9] proposed a two-step detection method to diagnose buckling damages in transmission towers. The first step consists of a wavelet packet energy curvature of the acceleration response of the structure to locate potential regions of buckling. Subsequently, the second step specifies the position of the buckled members through differences of modal strain energy change rates and confidence intervals. Overall, vibration-based buckling detection approaches are only applicable to cases where linearity remains valid, which is not the case in most buckling failures. A second group of approaches exploits the variations in the normal strains of structural members induced by the appearance of bending efforts at buckling [10]. A promising solution for buckling detection is the use of distributed strain fibre optic sensors [11]. Ravet *et al.* [12] reported the application of a Brillouin sensor system to identify buckling in a steel pipe and a column specimen under laboratory conditions. Similarly, Feng *et al.* [13] proposed the use of Brillouin fibre optic sensors for lateral buckling detection in subsea pipelines. Fibre Bragg Grating sensors (FBG) were used by Ryu *et al.* [14] to monitor the buckling behaviour of a composite wing box. Embedded into the structural components of the structure, these sensors provide distributed stress and strain measurements that permits detecting bending-induced strains derived from buckling. Other innovative solutions include the use of piezoelectric transducers [15], Frequency Selective Surfaces (FSS) [16], or Digital Image Correlation (DIC) measurements [17].

Novel multifunctional materials, such as smart concretes or self-sensing polymer composites, offer an innovative monitoring alternative with a vast spectrum of applications for SHM [18]. Commonly, these smart composites are enriched with carbon-based inclusions, such as carbon black, carbon nanofibers, Carbon NanoTubes (CNTs) or graphene nanoplatelets [19–21]. When added in small concentrations and adequately dispersed, such fillers have been reported to confer remarkable mechanical improvements to cement-based and polymer materials, as well as multifunctional properties including enhanced electrical conductivity and self-sensing capacities [22, 23]. Self-sensing capabilities manifest as measurable variations in the electrical properties of the composites when subjected to mechanical deformations, that is to say, a piezoresistive behaviour.

Three main strands of integration of self-sensing composites into large-scale structures for SHM can be found in the literature, namely structures completely made of smart materials [24], embedded sensors [25], and self-sensing skins [26]. Although the development of fully smart structures provides a comprehensive monitoring of their integrity, the high costs of the fillers and complex current fabrication processes related to their dispersion hinder the extensive implementation of these solutions [27]. Alternatively, the application of smart composites in the shape of embedded small-dimensions sensors forming dense sensing networks offers a more cost-efficient solution. Naeem *et al.* [28] analysed the stress and crack sensing capabilities of cement-based composites doped with Multi Walled CNT (MWCNT) under flexural loadings. Those authors manufactured prismatic embeddable sensors with different geometries, including smart sensors of 50x50x50 mm^3, 160x40x40 mm^3 and 1500x15x15 mm^3. When embedded into steel-reinforced mortar beams, their results reported steep increases in the electrical resistance of the sensors indicating the appearance of flexural cracks in the host structure. More recently, Downey *et al.* [29] proposed a novel piezoresistive clay brick for crack detection applications in masonry structures. While promising, the implementation of embedded sensors is limited to new-construction structures, being difficult their deployment into pre-existing structures. As an intermediate solution, the development of smart piezoresistive skins offers a cost-efficient alternative for the health monitoring of pre-existing structures. In virtue of their piezoresistive properties, it is possible to relate the monitored strain state to the presence of damages in the host structure. In this line, it is worth noting the works by Kang *et al.* [30] who developed 10wt.% MWCNT-reinforced Poly(methyl methacrylate) (PMMA) strain sensors. Under laboratory conditions, the authors bonded MWCNT/PMMA sensors with dimensions 50x4x0.08 mm^3 to an aluminium cantilever using a spray-on technique. Their results demonstrated the ability of the sensing strips for damage localization of prescribed damages. Although great efforts have been done from experimentation, there is no a generalized theoretical approach allowing a proper understanding of the output of the sensors, as well as assisting their design and optimization.

The modelling of the behaviour of CNT-based composites for SHM applications is in essence a multiscale-multiphysics problem. Considering that piezoresistance defines a one-way coupled electrical–mechanical property, it is possible to conduct the homogenization of the mechanical and electrical properties of CNT-based composites in two consecutive steps. Firstly, the mechanical properties of CNT-based composites have been reported to be determined by the load transfer mechanisms from matrix to fillers at the nano-scale. Such interactions are defined by weakly non-bonded van der Waals (vdW) interatomic potentials [31]. Hence, the mechanical homogenization of CNT-based composites is formulated in a bottom-up multi-scale framework where the atomic

interactions must be scaled up to the macro-scale. In this regard, the most common approaches in the literature include [32]: Molecular Dynamics (MD) simulations, atomistic-based continuum modelling, and mean-field homogenization with interfacial effects. Molecular dynamics simulations permit the study of the atomic structure of CNTs and their interaction with the matrix material [33]. Since realistic systems with a representative number of atoms demand exorbitant computational costs, MD simulations are generally well-suited to investigate local effects in reduced populations of atoms. Atomistic-based continuum techniques assume certain relations between the interatomic potentials and the stiffness of continuum structures such as truss rods or link elements. In this way, it is possible to describe the atomistic structure of the composite through a continuum framework such as Finite Element (FE) modelling with moderate computational costs [34]. Finally, mean-field homogenization approaches with interfacial effects offer a simplified alternative by considering the load transfer mechanisms as certain mechanical conditions at matrix/CNT interfaces [35–37].

The second step of the homogenization of the constitutive properties of CNT-based composites concerns the electrical conductivity and piezoresistivity. The electrical conductivity of these composites has been widely depicted through a percolative-type behaviour [38, 39]. This achieves to explain the sudden increases in the overall electrical conductivity of CNT-based composites when the filler concentration reaches a critical value, termed percolation threshold [40, 41]. A noteworthy contribution was made by Feng and Jiang [42] who proposed a Mori-Tanaka micromechanics model in the framework of percolation theory for CNT/polymer composites. That model distinguished two conductive mechanisms, namely the electron hopping (quantum tunnelling effect) and conductive networking mechanisms. The electron hopping mechanism, which defines the transfer of electrons between proximate nanotubes across an isolating gap, was modelled by conductive coatings surrounding the tubes. On the other hand, the conductive networking mechanism, which alludes to the appearance of microscopic conductive paths of interconnected nanotubes, was simulated by changes in the fillers' aspect ratios. Those authors demonstrated that the conductive networking mechanism represents the onset of the percolation process and, above the percolation threshold, both mechanisms govern the overall conductivity of composites. Concerning the piezoresistivity of CNT-based composites, the number of works is considerably lower. Most studies agree to ascribe their self-diagnostic capabilities to strain-induced disturbances in the electron hopping and conductive networking mechanisms [43]. In particular, three major alterations are typically identified [38, 44, 45]: (i) decrease of the apparent filler content during volume expansion of composites, (ii) reorientation of fillers, and (iii) changes in the inter-particle properties. In this light, Alamusi and Hu [46] proposed a three-dimensional resistor network model incorporating the tunnelling effect of CNTs along with the fillers' reorientation. Tallman and Wang [44] proposed a simplified analytical piezoresistivity model on the basis of the excluded volume approach for CNT-based composites subjected to arbitrary dilations. Afterwards, Feng and Jiang extended their Mori-Tanaka micromechanics model [42] to account for uni-axial [38] and bi-axial [47] stretching sensitivity. Interestingly, those authors proposed a fillers' reorientation model based on closed-form strain-dependent Orientation Distribution Functions (ODFs). Later, the authors proposed a mixed Mori-Tanaka pierosistivity model for cement-based composites doped with CNTs under uni-axial [45] and, more recently, arbitrary three-dimensional strain states [48]. As an extension of Feng and Jiang's model, the reorientation ODFs were also used to compute the strain-induced variation of the percolation threshold through a stochastic percolation model.

In view of the literature review, this paper presents a numerical study on the application of MWCNT/epoxy composites for buckling detection in beam-like structures in the realm of SHM. In particular, a novel smart beam is proposed consisting of a pristine epoxy beam equipped with two MWCNT/epoxy sensing strips attached onto its outer faces. Epoxy is selected as matrix material for the sensing strips due to its relatively low unit cost and facile processing, allowing designing sensors with a variety of geometries adaptable to pre-existing structures. The failure detection mechanism of the proposed smart beams consists of the detection of the buckling-induced bending strains through continuous monitoring of the electrical resistance of the sensing strips. The proposed devices can be installed in large-scale spatial structures at critical locations for timely buckling detection. In this way, it is possible to detect local buckling failures and assist the decision-making of corrective actions to prevent them from progressing into a global failure. The contribution of the present work is twofold: application of a micromechanics-based FE model for the electromechanical analysis of MWCNT/epoxy strip-like sensors, and analysis of the potential application of the proposed smart beams for buckling detection. To do so, the mechanical properties of the composites are computed by a core-shell micromechanics model. Afterwards, the piezoresistivity properties are computed by the generalized piezoresistivity model proposed by the authors in reference [48]. For validation purposes, the theoretical estimates are benchmarked against experimental data retrieved from the literature. The computed constitutive properties are used to study the macroscopic response of uniaxially compressed smart beams through an electromechanical numerical analysis in the commercial FE code ANSYS. Finally, a two-probe resistivity measurement scheme is proposed to detect buckling-induced disturbances in the electrical output of the sensors. The numerical results demonstrate that the buckling of the beams can be inferred from the electrical output of the smart beams, and detailed parametric analyses are presented to investigate

the influence of the micromechanical variables in the electromechanical response of the smart beams.

The paper is organized as follows: Section 2 introduces the proposed concept of smart beams consisting of MWCNT/epoxy sensing strips deployed on host pristine epoxy beams. Section 3 overviews the modelling of the electromechanical response of the smart beams through a micromechanics-based FE modelling. Section 4 presents the numerical results and discussion and, finally, Section 5 concludes the paper.

2. Smart CNT/epoxy beams for buckling failure detection

The proposed concept of smart beams for buckling failure detection is illustrated in Fig. 1. This consists of a beam of length L, width B, and thickness h_n with two MWCNT/epoxy strip-like sensors of thickness h_s attached onto the top and bottom surfaces of the beam. The total depth of the smart beam is denoted with h. In this work, the electromechanical behaviour of the proposed smart beams is investigated under uni-axial compression loads P through a 2D plane-strain approach ($\varepsilon_{zz} \approx 0$).
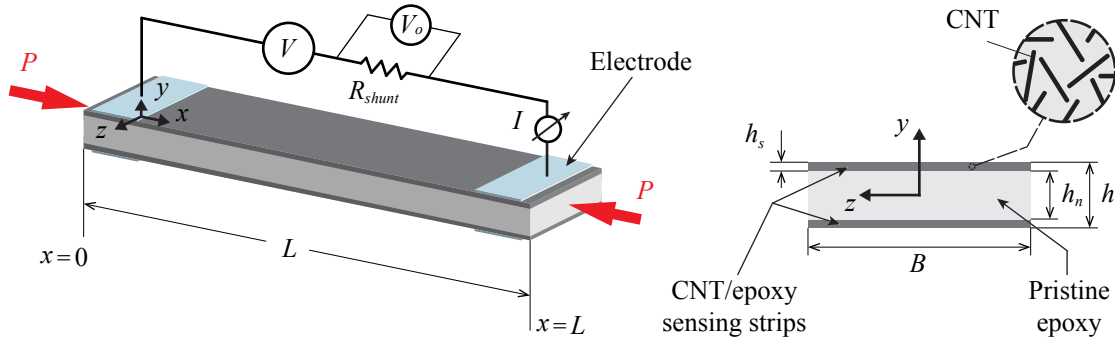

Figure 1: Schematic representation of smart CNT-reinforced beams and electric resistivity measurement scheme.

The mechanical response of a uniaxially compressed beam-like structure is well-known to follow an initial linear shortening until a critical load, termed critical buckling load, at which the beam becomes unstable and experiences sudden non-linear transverse displacements, that is to say, a buckling failure. The initiation of buckling implies the appearance of bending efforts due to the displacement of the neutral axis of the beams. Given their localization, buckling also induces variations of the longitudinal strains of the smart strips and, as a consequence, alterations of their electrical properties. Therefore, the proposed smart beams leverage the strain sensing capabilities of MWCNT-based composites to detect buckling failures through bending-induced disturbances in the electrical outputs of the sensing strips. To do so, the measurement scheme for each smart strip consists of a two-probe resistivity measurement as sketched in Fig. 1. Two superficial electrodes (e.g. copper foil or conductive paint) are mounted on each strip at the extremes of the beam, and shunt resistors R_{shunt} are linked between the power sources and the first electrodes, while the second ones are grounded. Monitoring the voltage drop across one of the shunt resistors V_o, the electric current I flowing through the sensor can be readily computed as $I = V_o/R_{shunt}$. Afterwards, the electrical resistance between electrodes is simply calculated by dividing the remaining voltage by the measured electric current as:

$$R = \frac{V - V_o}{I} \tag{1}$$

In this way, the MWCNT/epoxy sensing strips simultaneously act as mechanical reinforcements and provide self-diagnostic properties to the host beams. In practice, the measurement system can be solely implemented in one of the sensing strips if desired. Nonetheless, it is important to implement both strips in slender beams in order to avoid asymmetric stiffnesses that may accelerate the instability process. With regard to the electrical response of the sensing strips, self-sensing composite materials doped with carbon nano-inclusions have been reported to exhibit an inherent time-based drift in their electrical output when supplied with Direct Current (DC) voltage [49]. This drift is characterized by an increase in the resistance in time, often termed polarization. As a solution, it has been reported in the literature that the use of Alternating Current (AC) power sources minimizes this drift [50]. A noticeable alternative is the biphasic DC resistivity measurement approach proposed by Downey and co-authors [51, 52] for cement-based composites doped with MWCNTs. Applying periodic measure/discharge square waves, those authors demonstrated that DC resistivity measurements during the measurement regions provides stable readings in time. Therefore, theoretical simulations limited to the steady-state response of the system are consistent with currently available technical possibilities.

4

3. Micromechanics-based FE electromechanical modelling of smart beams equipped with MWCNT/epoxy sensing strips

In this section, the electromechanical constitutive properties of MWCNT/epoxy sensing strips are computed by a mixed micromechanics approach. Then, the macroscopic response of uniaxially compressed smart beams are modelled by means of a micromechanics-based FE approach. For notational convenience, blackboard bold letters are used to denote fourth-order tensors, while bold letters indicate second-order tensors.

3.1. Elastic properties of MWCNT-reinforced composites

The elastic moduli of MWCNT/epoxy composites are computed by a core-shell micromechanics approach [36, 37]. This model, also termed interphase model, assumes that interfacial properties can be idealized as finite elastic coatings with constant thickness t surrounding the fillers as shown in Fig. 2. Let us define a Representative Volume Element (RVE) of a linear elastic matrix doped with a sufficient number of MWCNTs to statistically represent the composite. The geometrical dimensions of MWCNTs, that is length L_{cnt} and diameter D_{cnt}, are assumed constant throughout the RVE. In order to describe the orientation of the fillers, two Euler angles, θ and γ, are defined to determine the orientation of the local coordinate system $K' \equiv \left\{0; x_1' x_2' x_3'\right\}$ at every MWCNT. According to the interphase model, the material is defined as a three-phase composite including the host matrix, inclusions and surrounding interphases with elastic tensors $\mathbb{C}_m$, $\mathbb{C}_p$ and $\mathbb{C}_i$, respectively. Subscripts "p", "i", and "m" relate the corresponding quantity to the filler, interphase and matrix, respectively. In accordance with the notation of Hori and Nemat-Nasser [53], every MWCNT and its surrounding interphase define a double inclusion, and the effective constitutive tensor of the composite reads:
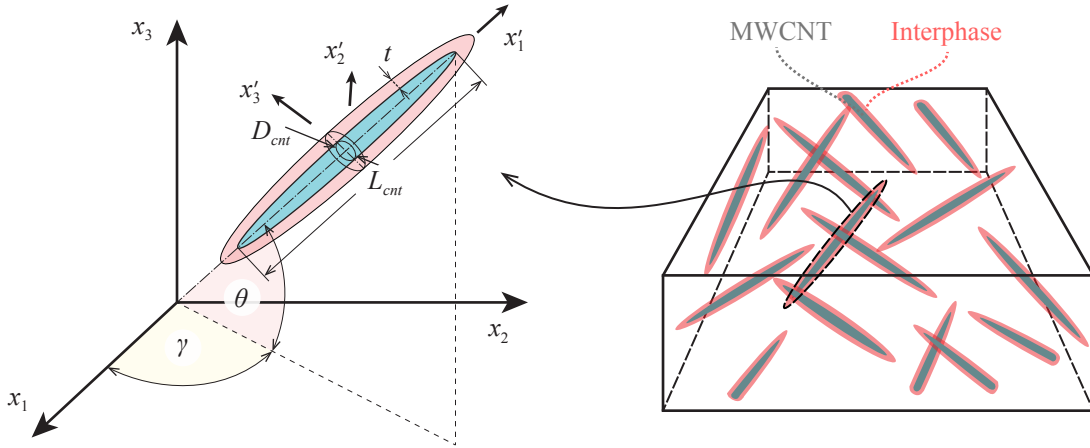

Figure 2: Euler angles defining the relation between the orientation of a MWCNT in the local coordinate system, $K' \equiv \left\{0; x_1' x_2' x_3'\right\}$ and the global coordinate system, $K \equiv \{0; x_1 x_2 x_3\}$.

$$\overline{\mathbb{C}} = \left(f_m \mathbb{C}_m + f_i \left\langle \mathbb{C}_i : \mathbb{A}_i \right\rangle + f_p \left\langle \mathbb{C}_p : \mathbb{A}_p \right\rangle\right) : \left(f_m \mathbb{I} + f_i \left\langle \mathbb{A}_i \right\rangle + f_p \left\langle \mathbb{A}_p \right\rangle\right)^{-1} \tag{2}$$

with f_p, f_i, and f_m being the volume fraction occupied by the fillers, the interphases and the host matrix, respectively. A colon between two tensors denotes tensorial inner product, $(\mathbb{A} : \mathbb{B})_{ijmn} \equiv A_{ijkl} B_{klmn}$. The terms $\mathbb{A}_i$ and $\mathbb{A}_p$ stand for the concentration tensors for interphases and inclusions, respectively, and can be expressed in terms of the corresponding dilute concentration tensors, $\mathbb{A}_i^{dil}$ and $\mathbb{A}_p^{dil}$, as:

$$\mathbb{A}_\chi = \mathbb{A}_\chi^{dil} : \left(f_m \mathbb{I} + f_i \mathbb{A}_i^{dil} + f_p \mathbb{A}_p^{dil}\right)^{-1}, \quad \chi = p, i \tag{3}$$

$$\mathbb{A}_\chi^{dil} = \mathbb{I} + \mathbb{S} : \mathbb{T}_\chi, \quad \chi = p, i \tag{4}$$

with

$$\mathbb{T}_\chi = -\left(\mathbb{S} + \mathbb{M}_\chi\right)^{-1}, \quad \chi = p, i \tag{5}$$

$$\mathbb{M}_\chi = \left(\mathbb{C}_\chi - \mathbb{C}_m\right)^{-1} : \mathbb{C}_m, \quad \chi = p, i \tag{6}$$

5

Angle brackets operators in Eq. (2) represent orientational average. The orientational average of any function $F(\gamma, \theta)$, i.e. $\langle F \rangle$, is defined through:

$$\langle F \rangle = \int_0^{2\pi} \int_0^{\pi/2} F(\gamma, \theta) \Omega(\gamma, \theta) \sin(\theta) \mathrm{d}\theta \mathrm{d}\gamma \tag{7}$$

with $\Omega(\gamma, \theta)$ being the so-termed Orientation Distribution Function. Unless special aligning techniques are adopted, the fillers are randomly oriented throughout the composite. In this case, the ODF is defined constant within the whole Euler space and of value $\Omega(\gamma, \theta) = 1/2\pi$.

Finally, the volume fraction of the interphases, f_i, remains to be defined. Generally, approaches disregarding the interfacial effects of MWCNT-based composites may lead to severe overestimations of the overall elastic properties [32]. This fact evidences the existence of compliant MWCNT/matrix interface zones due to weakly non-bonded vdW forces. Compliant interfaces typically possess low stiffness and can be considered as penetrable interphases surrounding the fillers. Xu *et al.* [54] derived the expression of the volume fraction of finite soft interphases around monodisperse ellipsoidal particles as:

$$f_i = (1 - f_p)\left(1 - \exp\left\{-\frac{6 f_p}{1 - f_p}\left[\frac{\eta}{n(\kappa)} + \left(2 + \frac{3 f_p}{n^2(\kappa)(1 - f_p)}\right)\eta^2 + \right.\right.\right.$$
$$\left.\left.\left. + \frac{4}{3}\left(1 + \frac{3 f_p}{n(\kappa)(1 - f_p)}\right)\eta^3\right]\right\}\right) \tag{8}$$

where term η denotes the ratio of the thickness of the interphases t and the equivalent diameter D_{eq} (i.e. $\eta = t/D_{eq}$). The equivalent diameter, which defines the diameter of an equivalent sphere having the same volume as that of the particles [55], can be expressed for MWCNTs with aspect ratio $\kappa = L_{cnt}/D_{cnt} > 1$ as $D_{eq} = D_{cnt}\kappa^{1/3}$. The term $n(\kappa)$ stands for the sphericity of the fillers and is defined as the ratio between the surface area the equivalent sphere and that of the particles, that is:

$$n(\kappa) = \frac{2\kappa^{2/3} \tan\varphi}{\tan\varphi + \kappa^2\varphi} \tag{9}$$

where φ is given by $\varphi = \arccos(\beta)$, with $\beta = 1/\kappa$.

3.2. Electrical conductivity of unstrained MWCNT-based composites

On the basis of the percolative-type behaviour of MWCNT-based composites, the overall electrical conductivity experiences a rapid increase when the filler concentration reaches the percolation threshold f_c. Below percolation ($f_p < f_c$), fillers are very distant and the transfer of electrons is only possible through the electron hopping mechanism. Conversely, once the MWCNT volume fraction reaches the percolation threshold ($f_p \geq f_c$), some fillers begin forming conductive networks and the overall conductivity is governed by both electron hopping and conductive networking mechanisms as schematically represented in Fig. 3. Hence, the fraction of percolated MWCNTs, ξ, can be approximately estimated as [40]:

$$\xi = \begin{cases} 0, & 0 \leq f_p < f_c \\ \dfrac{f_p^{1/3} - f_c^{1/3}}{1 - f_c^{1/3}}, & f_c \leq f_p \leq 1 \end{cases} \tag{10}$$
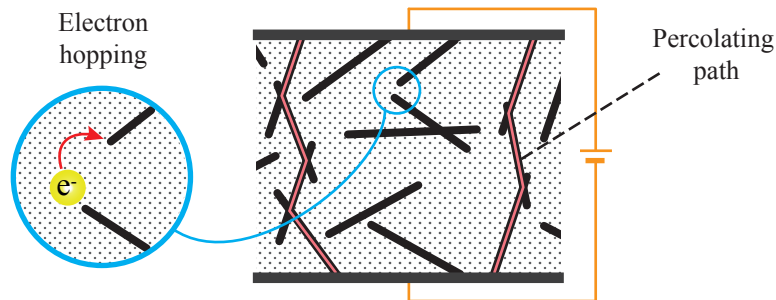

Figure 3: Schematic representation of the contribution of electron hopping and conductive networking mechanisms to the overall electrical conductivity of CNT nanocomposites.

6

The electron hopping mechanism can be modelled by a conductive interphase surrounding the nanotubes, whilst the conductive networking mechanism can be simulated by variations of the filler's aspect ratio [42]. In the first case, the electrical resistivity of the interphases is commonly computed by the generalized Simmons' formula as follows [56]:

$$R_{int}(d_a) = \frac{d_a \hbar^2}{ae^2 (2m\lambda^{1/2})} \exp\left(\frac{4\pi d_a}{\hbar} (2m\lambda)^{1/2}\right) \tag{11}$$

where m and e are the mass and the electric charge of an electron, respectively, λ is the height of the tunnelling potential barrier, a is the contact area of the MWCNTs, and $\hbar$ stands for the reduced Planck's constant. The term d_a denotes the average distance between MWCNTs without electrical contacts and is usually defined in a piecewise form as follows [42]:

$$d_a = \begin{cases} d_c & 0 \le f_p < f_c \\ d_c \left(\dfrac{f_c}{f_p}\right)^{1/3} & f_c \le f_p \le 1 \end{cases} \tag{12}$$

with d_c standing for the cut-off distance for tunnelling effects, that is, the maximum separation between MWCNTs in which the tunnelling penetration of electrons can take place. On this basis, the thickness of the conductive interphases t_c, their electrical conductivity σ_{int}, and the volume fraction f_{eff} of the effective solid fillers (fillers and interphases) can be computed as [42, 57]:

$$t_c = \frac{1}{2}d_a, \quad \sigma_{int} = \frac{d_a}{aR_{int}(d_a)}, \quad f_{eff} = \frac{(D_{cnt} + 2t_c)^2 (L_{cnt} + 2t_c)}{D_{cnt}^2 L_{cnt}} f_p \tag{13}$$

The properties of the conductive interphases determine the transversely isotropic conductivity tensor of equivalent solid cylinders, $\boldsymbol{\sigma}_c$ (see references [42, 58] for more details). Hence, the Mori-Tanaka estimation of the overall electrical conductivity of a RVE of a polymer matrix of electrical conductivity σ_m doped with a sufficient number of fillers with conductivity $\boldsymbol{\sigma}_c$ can be defined as follows [59]:

$$\boldsymbol{\sigma}_{eff} = \sigma_m + (1 - \xi)\langle \Gamma_{EH} \rangle + \xi \langle \Gamma_{CN} \rangle \tag{14}$$

with:

$$\Gamma_{EH} = f_{eff} (\boldsymbol{\sigma}_{EH} - \sigma_m) \boldsymbol{A}_{EH} \tag{15a}$$

$$\Gamma_{CN} = f_{eff} (\boldsymbol{\sigma}_{CN} - \sigma_m) \boldsymbol{A}_{CN} \tag{15b}$$

where subscripts *EH* and *CN* refer to electron hopping and conductive networking mechanisms, respectively. In the case of CNTs forming conductive networks, several nanotubes are electrically connected in a continuous conductive path. This effect can be modelled by considering fillers with infinite aspect ratio [57]. As a result, the quantities associated with the electron hopping mechanism are defined with the real fillers aspect ratio ($\kappa = L_{cnt}/D_{cnt}$), while quantities corresponding to conductive networks are defined with an infinite aspect ratio ($\kappa \to \infty$). Finally, the electric field concentration tensor, $\boldsymbol{A}$, can be expressed as [42]:

$$\boldsymbol{A} = \boldsymbol{A}^{dil} \left\{ \left(1 - f_{eff}\right)\boldsymbol{I} + f_{eff} \left\langle \boldsymbol{A}^{dil} \right\rangle \right\}^{-1} \tag{16}$$

with $\boldsymbol{A}^{dil}$ being the dilute electric field concentration tensor:

$$\boldsymbol{A}^{dil} = \left\{ \boldsymbol{I} + \boldsymbol{S} (\sigma_m)^{-1} (\boldsymbol{\sigma}_c - \sigma_m) \right\}^{-1} \tag{17}$$

where $\boldsymbol{I}$ is the second-order identity tensor and $\boldsymbol{S}$ the Eshelby's tensor, well documented in [60].

Finally, it is important to note that this micromechanics approach offers a suitable framework for including waviness and agglomeration effects. Details on the formulation of these two phenomena have been omitted in this work due to space constraints. For more information on this aspect, readers are invited to read Sections 2.2 and 2.3 in reference [45].

3.3. Strain-induced alterations in the overall conductivity of MWCNT-based composites

On the basis of the previously overviewed micromechanics model, the strain-sensing capabilities of MWCNT-based composites can be simulated by means of strain-induced tampering of the electron hopping and conductive networking mechanisms. In the following, the modelling of the three major strain-induced effects proposed by the authors in reference [48] is concisely presented here, including the volume expansion and reorientation of MWCNTs, variation of the percolation threshold, and variation of the inter-particle properties.

7

3.3.1. Volume expansion and reorientation of MWCNTs

The volume expansion and reorientation of fillers is independently studied under dilation and distortion strains. To do so, a deformable cubic cell of side l_o containing an embedded filler is defined as sketched in Fig. 4 (a). Firstly, the deformable cell is studied under the application of an arbitrary 3D strain state $(\varepsilon_1, \varepsilon_2, \varepsilon_3)$ as shown in Fig. 4 (b). The volume of the cell changes from $V_o = l_o^3$ to $V_\varepsilon = l_o^3 (1 + \varepsilon_1)(1 + \varepsilon_2)(1 + \varepsilon_3) = l_o^3 \overline{\varepsilon}_1 \overline{\varepsilon}_2 \overline{\varepsilon}_3$. Since fillers are considerably stiffer than the matrix, the deformation of the composite is mainly sustained by the matrix and, as a result, the apparent filler content varies as follows:

$$f^* = \frac{V_o f}{V_\varepsilon} = \frac{f}{\overline{\varepsilon}_1 \overline{\varepsilon}_2 \overline{\varepsilon}_3} \tag{18}$$
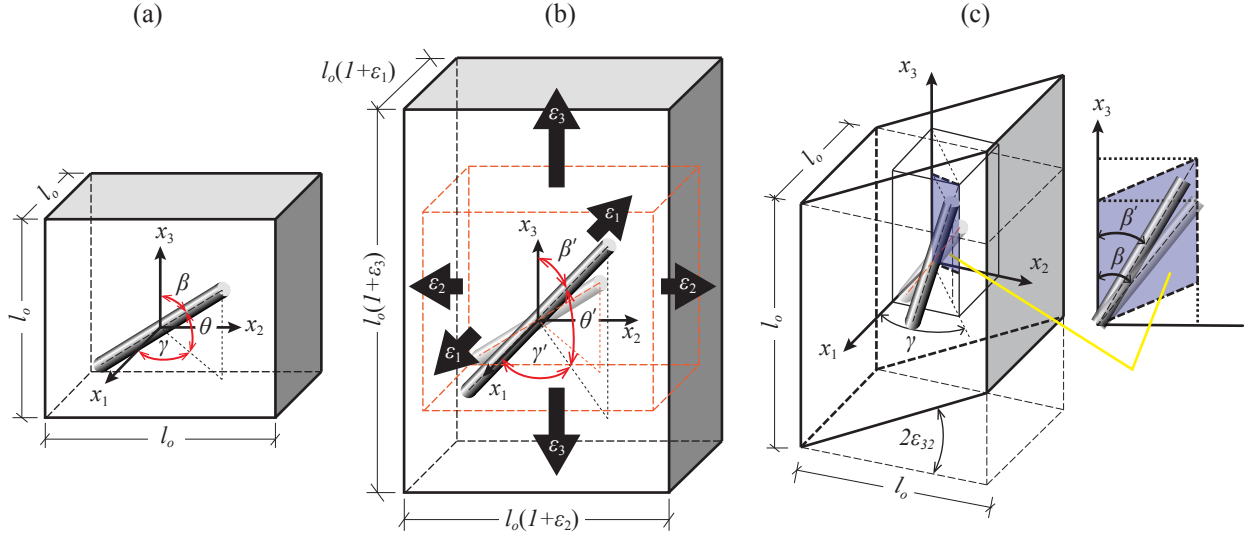

Figure 4: Deformable cubic cell containing an embedded filler (a), deformed cell under a triaxial strain state $(\varepsilon_1, \varepsilon_2, \varepsilon_3)$ (b), and deformed cell under a distortion ε_{32}.

Likewise, the application of dilations also originates reorientation of the fillers. Such reorientation is characterized by a change of the Euler angles from (γ, β) to (γ', β') as shown in Fig. 4 (b). The closed-form expression of the strain-dependent ODF under three-dimensional dilation strains, $\Omega(\gamma', \beta')$, was recently reported by the authors in reference [48] as:

$$\Omega(\gamma', \beta') = \frac{\overline{\varepsilon}_1^2 \overline{\varepsilon}_2^2 \overline{\varepsilon}_3^2}{\left[\overline{\varepsilon}_2^2 \overline{\varepsilon}_3^2 \cos^2 \beta' + \overline{\varepsilon}_1^2 \left(\overline{\varepsilon}_2^2 \cos^2 \gamma' + \overline{\varepsilon}_3^2 \sin^2 \gamma' \right) \sin^2 \beta' \right]^{3/2}} \tag{19}$$

Secondly, the deformable cell is studied under the application of a distortion ε_{32} as shown in Fig. 4 (c). In this case, distortion does not originate volume expansion although it does induce reorientation of fillers. In the particular case of ε_{32}, the polar angle changes from β to β', while the azimuthal angle remains unchanged. The closed-form expression of the resulting ODF was also reported by the authors in reference [48] as:

$$\Omega(\gamma, \beta') = \left(1 - 4\varepsilon_{32} \sin \gamma \sin \beta' \cos \beta' + 4\varepsilon_{32}^2 \sin \gamma \sin \beta' \right)^{-3/2} \tag{20}$$

3.3.2. Strain-induced variations of the percolation threshold

The strain-induced reorientation of fillers decreases the randomness of the MWCNTs' dispersion and, as a consequence, the likelihood of forming conductive networks also decreases. In other words, the reorientation of fillers leads to increasing percolation thresholds. Such variation can be expressed in terms of the previously outlined strain-dependent ODFs as shown by the authors in reference [45]. To do so, the stochastic percolation model of Komori and Makishima [61] can be used. According to this model, each filler must have at least two contact points to be part of a conductive path. Alternatively, the mean distance between contacts, $\overline{b}$, must be at least half the filler length. The mean distance between contacts $\overline{b}$ is given by [61]:

$$\overline{b} = \frac{\pi D_{cnt}}{8 I f_p} \tag{21}$$

where

8

$$I = \int_0^\pi \mathrm{d}\theta \int_0^\pi J(\gamma, \theta) \Omega(\gamma, \theta) \sin\theta \mathrm{d}\gamma \qquad (22)$$

$$J(\gamma, \theta) = \int_0^\pi \mathrm{d}\theta' \int_0^\pi \sin\tau \Omega(\gamma', \theta') \sin\theta' \mathrm{d}\gamma' \qquad (23)$$

$$\sin\tau = \left[1 - \{\cos\theta\cos\theta' + \cos(\gamma - \gamma')\sin\theta\sin\theta'\}^2\right]^{1/2} \qquad (24)$$

Following the work of Kumar and Rawal [62], the percolation threshold of the deformed composite can be expressed in terms of these quantities as:

$$f_c = \frac{\pi}{5.77\kappa I} \qquad (25)$$

In this way, it is possible to compute the strain-induced variations of the percolation threshold by introducing the ODFs from Eqs. (19) and (20) into Eq. (22) and using Eqs. (21) and (25).

3.3.3. Strain-induced alternations of the inter-particle properties

Externally applied mechanical strains also alter the separation among fillers and, therefore, the electron hopping mechanism is also affected. In particular, assuming that deformations are mainly sustained by the compliant matrix, mechanical strains primarily affect the inter-particle distance and the height of the potential barrier. At relatively low strains ($< 10^{-4}$), some research studies in the literature assume that the inter-particle distance, d_a, and the height of the potential barrier, λ, vary linearly with strain as follows [63]:

$$\begin{aligned} d_a &= d_{a,0}(1 + C_1\varepsilon), \\ \lambda &= \lambda_0(1 + C_2\varepsilon) \end{aligned} \qquad (26)$$

where $d_{a,0}$ and λ_0 denote the inter-particle distance and potential height of the unstrained system, respectively, and C_1 and C_2 are proportionality constants. The explicit determination of the relation between these magnitudes and mechanical strains is an intricate task. On one hand, these effects take place between nanotubes at the nano-scale through inter-atomic interactions. On the other hand, the study of the influence of such effects on the macro-scale should be coped through the analysis of computationally intensive RVEs or, alternatively, through stochastic upscaling approaches. Such studies remain unexplored and, given the lack of information in the literature, the proportionality constants C_1 and C_2 are usually computed through the fitting of experimental data.

3.4. Piezoresistivity matrix of MWCNT-based composites

The modelling of the piezoresistivity of a MWCNT-based composite requires combining the equations governing its electrical behaviour with those describing the mechanical strain state. To do so, the overall electrical resistivity tensor, $\boldsymbol{\rho}_{eff}$, is first computed as the inverse of the conductivity tensor $\boldsymbol{\sigma}_{eff}$ defined in Eq. (14). For notational convenience, the electrical resistivity tensor is written in matrix notation as:

$$\boldsymbol{\rho}_{eff} = \begin{bmatrix} \rho_1 & \rho_6 & \rho_5 \\ \rho_6 & \rho_2 & \rho_4 \\ \rho_5 & \rho_4 & \rho_3 \end{bmatrix} \qquad (27)$$

When the composite is subjected to no strain, MWCNTs are randomly oriented throughout the composite and the electrical resistivity tensor takes the form of a scalar matrix with diagonal terms ρ_0, i.e. $\rho_1 = \rho_2 = \rho_3 = \rho_0$ and $\rho_4 = \rho_5 = \rho_6 = 0$. Once the composite is subjected to a mechanical strain, the components of the resistivity matrix change as follows:

$$\begin{bmatrix} \rho_1 \\ \rho_2 \\ \rho_3 \\ \rho_4 \\ \rho_5 \\ \rho_6 \end{bmatrix} = \begin{bmatrix} \rho_0 \\ \rho_0 \\ \rho_0 \\ 0 \\ 0 \\ 0 \end{bmatrix} + \begin{bmatrix} \Delta\rho_1 \\ \Delta\rho_2 \\ \Delta\rho_3 \\ \Delta\rho_4 \\ \Delta\rho_5 \\ \Delta\rho_6 \end{bmatrix} \qquad (28)$$

or in a more compact way:

$$\boldsymbol{\rho}_{eff} = \boldsymbol{\rho}_{eff}^o (\boldsymbol{I} + \boldsymbol{r}) \qquad (29)$$

9

where $\boldsymbol{\rho}_{eff}^o$ stands for the unstrained resistivity tensor. The term $\boldsymbol{r}$ denotes the tensor of relative change in resistivity and can be related to the mechanical strain tensor $\boldsymbol{\varepsilon}$ as $\boldsymbol{r} = \boldsymbol{\Pi}\boldsymbol{\varepsilon}$, with $\boldsymbol{\Pi}$ being the so-termed piezoresistivity matrix. Assuming that the piezoresistivity matrix of CNT-based composites possesses cubic crystal symmetry, similarly to piezoresistive silicon [64], this relation can be written in matrix notation as:

$$
\begin{bmatrix} \Delta\rho_1/\rho_0 \\ \Delta\rho_2/\rho_0 \\ \Delta\rho_3/\rho_0 \\ \Delta\rho_4/\rho_0 \\ \Delta\rho_5/\rho_0 \\ \Delta\rho_6/\rho_0 \end{bmatrix} = \begin{bmatrix} \lambda_{11} & \lambda_{12} & \lambda_{12} & 0 & 0 & 0 \\ \lambda_{12} & \lambda_{11} & \lambda_{12} & 0 & 0 & 0 \\ \lambda_{12} & \lambda_{12} & \lambda_{11} & 0 & 0 & 0 \\ 0 & 0 & 0 & \lambda_{44} & 0 & 0 \\ 0 & 0 & 0 & 0 & \lambda_{44} & 0 \\ 0 & 0 & 0 & 0 & 0 & \lambda_{44} \end{bmatrix} \begin{bmatrix} \varepsilon_1 \\ \varepsilon_2 \\ \varepsilon_3 \\ 2\varepsilon_{23} \\ 2\varepsilon_{13} \\ 2\varepsilon_{12} \end{bmatrix} \tag{30}
$$

where the terms λ_{ij} denote the components of the piezoresistivity matrix. Discussion on the correctness of the hypothesis of cubic crystal symmetry for CNT-based smart concretes was reported by the authors in reference [48]. Note that this assumption leads to only thee independent λ−coefficients in Eq. (30). Here, λ_{11} depicts the piezoresistive effect along one principal crystal axis for strains applied in the same axis (longitudinal piezoresistive effect), λ_{12} relates the piezoresistive effect along one principal crystal axis for strains applied in a perpendicular axis (transverse piezoresistive effect), and λ_{44} describes the piezoresistive effect on an out-of-plane electric field by the change of the in-plane current induced by in-plane shear strain. In order to compute the independent components of $\boldsymbol{\Pi}$, only two virtual experiments are needed, namely a laterally constrained uni-axial dilation test and a distortion test as follows [48]:

$$
\begin{bmatrix} \Delta\rho_1/\rho_0 \\ \Delta\rho_2/\rho_0 \\ \Delta\rho_3/\rho_0 \end{bmatrix} = \begin{bmatrix} \lambda_{11} & \lambda_{12} & \lambda_{12} \\ \lambda_{12} & \lambda_{11} & \lambda_{12} \\ \lambda_{12} & \lambda_{12} & \lambda_{11} \end{bmatrix} \begin{bmatrix} 0 \\ 0 \\ \varepsilon_3 \end{bmatrix} = \boldsymbol{\Pi}^{dil} \begin{bmatrix} 0 \\ 0 \\ \varepsilon_3 \end{bmatrix} \tag{31}
$$

$$
\begin{bmatrix} \Delta\rho_4/\rho_0 \\ \Delta\rho_5/\rho_0 \\ \Delta\rho_6/\rho_0 \end{bmatrix} = \begin{bmatrix} \lambda_{44} & 0 & 0 \\ 0 & \lambda_{44} & 0 \\ 0 & 0 & \lambda_{44} \end{bmatrix} \begin{bmatrix} 0 \\ 0 \\ 2\varepsilon_{12} \end{bmatrix} = \boldsymbol{\Pi}^{dis} \begin{bmatrix} 0 \\ 0 \\ 2\varepsilon_{12} \end{bmatrix} \tag{32}
$$

The piezoresistivity matrices under laterally constrained uni-axial dilation and distortion, $\boldsymbol{\Pi}^{dil}$ and $\boldsymbol{\Pi}^{dis}$, respectively, can be computed on the basis of the previously outlined micromechanics approach in Section 3.2, in combination with the strain-induced effects addressed in Section 3.3. As a simplification, the proportionality constants in the definition of the strain-induced effects on the inter-particle properties, viz., C_1 and C_2, are only computed in this work for the virtual experiment of laterally constrained uni-axial dilation, while these are assumed zero for distortion strains following the results reported in reference [48].

3.5. FE electromechanical modelling of uniaxially-compressed smart beams equipped with MWCNT/epoxy sensing strips

Once the electromechanical constitutive properties of the MWCNT/epoxy composite are computed through the previously overviewed micromechanics approach, the macroscopic response of the smart beams presented in Section 2 can be simulated by a FE multiphysics approach. In this work, the numerical studies are conducted with the commercial code ANSYS v15.0 [65]. In particular, the smart beams are modelled with plane strain elements as shown in Fig. 5. Importantly, all the numerical results are presented per unit width $B = 1$ m. The epoxy beams are modelled with standard structural plane elements PLANE182 [65]. This element type is a quadrilateral 4-nodes element with two in-plane translations per node. On the other hand, the sensing strips are modelled with the piezoresistive plane elements, PLANE223 [65]. This element type is a quadrilateral 4-nodes element with three degrees of freedom per node (two in-plane translations and an electric potential). Considering that the electrodes are much more conductive than the strip, it is assumed that the electrodes can be simulated as coupling conditions of constant voltage along the electrodes' length L_e. In addition, the electrodes are located at a variable distance d_e from the ends of the beam in order to evaluate different electrodes layouts. The shunt resistor is modelled with the general two-nodes circuit element CIRCU124.
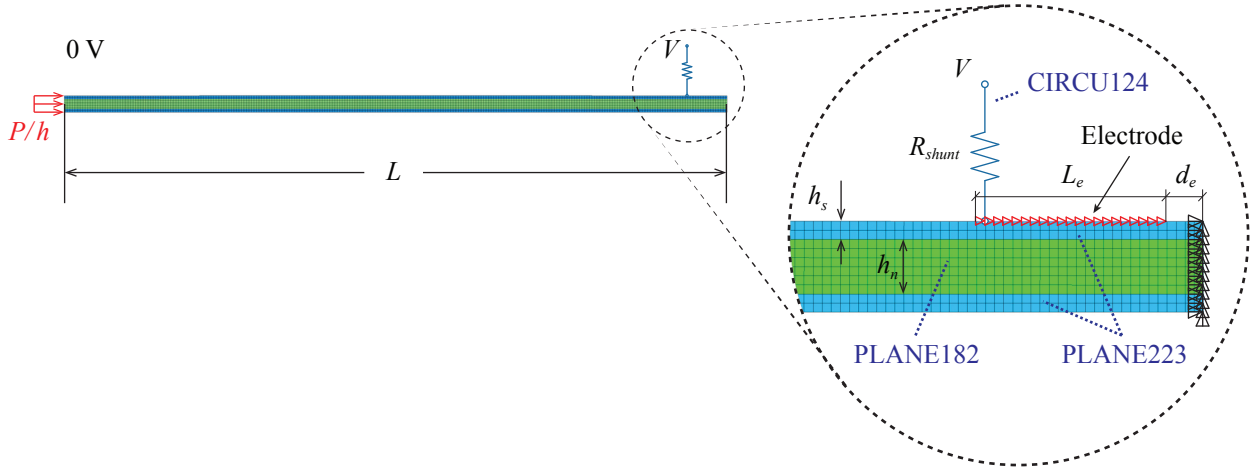
Figure 5: 2D FE model of smart a beam equipped with smart MWCNT/epoxy strip-like strain sensors.

In this light, the post-buckling behaviour of the smart beams is studied under uniaxial compressive loads
P. To do so, the loads are transferred into uniform pressure loads per unit length P/h across the cross-section
as shown in Fig. 5. The resulting forces depend upon the prescribed pressure magnitude and the orientation of
the cross-section, whereby the compressive forces can be defined as follower loads. The arc-length method is
adopted as solution strategy to trace the post-buckling bifurcation paths, being suitable for coping with complex
buckling behaviours such as secondary buckling, snap-back, or snap-through. Moreover, two boundary conditions
are investigated, namely simply supported (H-H) and fully clamped (C-C) conditions. Finally, in order to evaluate
the imperfection sensitivity of the beams, the geometry of the smart beams is modified including a geometric
imperfection with amplitude, A_o, in the transverse direction according to the first buckling mode.

4. Numerical results and discussion

In this section, the previously overviewed micromechanics-based FE modelling is utilized to model the smart
beams introduced in Fig. 1. To this aim, the section has been divided into two subsections, namely Subsection 4.1
and Subsection 4.2 concerning the determination of the electromechanical properties of CNT/polymer composites
and the analysis of the macro-response of the smart beams, respectively.

4.1. Effective properties of CNT/polymer sensing strips

In this subsection, the electrical and mechanical properties of CNT/polymer sensing strips are computed. For
this purpose, the micromechanics approaches presented in Subsections 3.1 and 3.2 are utilized to fit experimental
data. Firstly, the experimental results from references [23] and [22] are used as validation benchmarks. The
micromechanics variables have been fitted by means of a non-linear regression model. Afterwards, the mechanical
properties have been computed with the experimental results from reference [66] as a validation basis. In this
case, the stiffness and thickness of the interphases surrounding the CNTs have been also computed by a non-linear
regression fitting.

4.1.1. Electrical properties of CNT/polymer composites

Firstly, the micromechanical variables underlying the piezoresistive properties of CNT-reinforced polymers
have been fitted with the experimental results reported by Sanli *et al*. [23] as validation basis. To this end, the
micromechanics approach presented in Subsection 3.2 has been fitted by means of a non-linear regression model.
Eight micromechanical variables have been considered in the regression, including the length of the MWCNTs
($L_{cnt} \in [0.1 - 30]$ μm [38, 66, 67]), the diameter of the MWCNTs ($D_{cnt} \in [10 - 20]$ nm [38, 66]), the electrical
conductivity of the MWCNTs ($\sigma_c \in \left[10^1 - 10^4\right]$ S/m [42]), the mass density of the MWCNTs ($\rho_c \in [1.4 - 2.25]$
g/cm^3 [68]), the height of the potential barrier ($\lambda \in [0.5 - 2.5]$ eV [23]), and the proportionality constants C_1 and
C_2 ($C_1 \in [0 - 20]$, $C_2 \in [0 - 2]$). The Poisson's ratio, the mass density and the electrical conductivity of the epoxy
matrix are selected as constant values, ν_m=0.28, ρ_m=1.12 g/cm^3 [69] and σ_m=1.04E-10 S/m [22].

Firstly, the gauge factors computed by the present approach are fitted by those reported in reference [23] and
depicted in Fig. 6. In that work, the specimens where subjected to laterally unconstrained uni-axial stretching

11

$(\varepsilon_1, \varepsilon_2 = \varepsilon_3 = -\nu\varepsilon_1)$. The electrodes where defined perpendicular to the load application and, thus, the reported experimental gauge factors correspond to λ_{11} in Eq. (30). As previously evidenced in some other previously published experimental and theoretical works [70], the strain-sensing curves can be approximately modelled with a first linear range followed by a non-linear one. In this work, a linear regression based on a least squares estimator is adjusted in the strain range leading to a coefficient of determination of 0.99. In this way, the piezoresistivity coefficients are determined by the slope of the linear part of the curve relative variation of the electrical resistance versus applied strain ($\Delta R/R_o$ vs. ε). The fitted micromechanical variables are collected in Table 1, shown in the next subsection, and both the longitudinal and transverse piezoresistive coefficients are furnished in Fig. 6. It is first observed that very close agreements are found between the theoretical and the experimental results for λ_{11}. In accordance with previously published results, maximum values of piezoresistive coefficients are found for filler contents around the percolation threshold. Interestingly, it is also observed that the transverse piezoresistivity coefficient, λ_{12}, exhibits slightly higher values along the whole range of fibre concentrations. A similar behaviour has been also reported by some previously published experimental works on similar strain-sensing materials (see e.g. Fig. 10 in reference [29]).
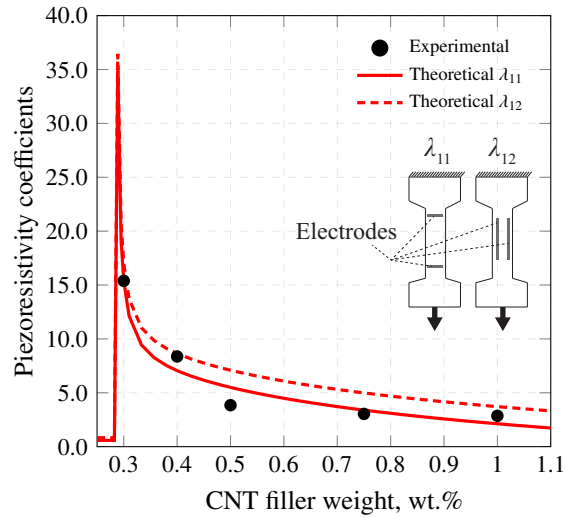

Figure 6: Piezoresistivity coefficients of MWCNT/epoxy composites versus filler concentration under laterally constrained uni-axial stretching (the experimental results have been taken from reference [23]).

The comparison between the strain sensing curves computed by the present theoretical approach and the experimental results reported by Sanli *et al.* [23] is shown in Fig. 7. The strain sensing curves are defined as the relative variation of the internal resistance $\left(\Delta R/R_o = \sigma_{eff}(\varepsilon = 0)/\sigma_{eff} - 1\right)$ versus the externally applied uni-axial stretching ε. In order to account for possible uncertainties related to the fabrication process of the different specimens, a non-linear regression model is also applied by considering the micromechanical parameters from Table 1 as initial guesses, and a range of variation of $\pm 2\%$. In addition, it is important to remark that all the fitted micromechanical variables in Table 1 have been assumed constant within all the range of filler contents. Nevertheless, micromechanical parameters such as the inter-particle distance d_a, the height of the potential barrier λ, or the proportionality constants C_1 and C_2, are presumably functions of the filler volume fraction. Due to the lack of information in the literature in this regard, the defined variation of $\pm 2\%$ is hypothesized to account for such variations. The results have been divided into filler volume fractions far and close from the percolation threshold in Figs. 7 (a) and (b), respectively. It is important to note that non-linearities, related to the coupled effect of the volume expansion and variation of the percolation threshold, gain importance for concentrations close to the unloaded percolation threshold (Fig. 7 (b)). In this case, the present approach shows a similar tendency, and the appearance of non-linearities is justified by the piecewise definition of the percolation theory (see Eq. (14)). Nonetheless, the results computed by the present approach with the fitted parameters from Table 1 fail to reproduce such high non-linearity degrees, and considerable discrepancies with the experimental data can be observed in Fig. 7 (b). The piezoresistive behaviour of CNT-based composites doped with filler contents close to the percolation threshold is highly sensible to inter-particle contact properties. Hence, these discrepancies may be due to the consideration of constant micromechanical variables for all the range of filler contents. Also, the definition of the strain-induced variations of the percolation threshold by means of ODFs may result in inaccurate results for such concentrations. On the contrary, the strain-sensing curves exhibit more linear behaviours for concentrations far from this critical concentration as shown in Fig. 7 (a). In this case, it is observed that the present approach

12

provides very close agreements with the experimental data. Linear transducers (Fig. 7 (a)) are of high interest in the realm of SHM because they provide more accurate measurements. Therefore, the scope of this work limits to linear smart sensors for which, in view of the previously reported results, the present approach has been shown acceptable.

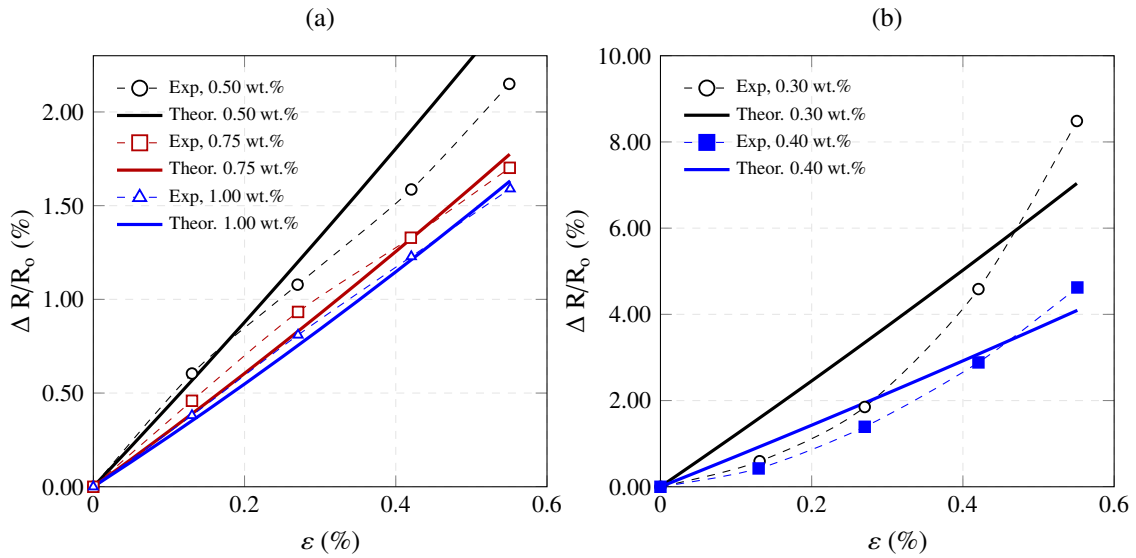Figure 7: Strain-induced relative resistance change $\Delta\rho/\rho_o$ of MWCNT/epoxy composites for filler volume fractions far (a) and close from the percolation threshold (b) under laterally constrained uni-axial stretching (the experimental results have been taken from reference [23]).

Finally, Fig. 8 shows the comparison of the theoretical predictions on the overall electrical conductivity of MWCNT/epoxy composites and the experimental results reported by Pilawka *et al.* [22]. The micromechanical variables used in the simulation have been taken from Table 1. For illustrative purposes, the theoretical estimates with a filler conductivity of $\sigma_c = 10^3$ S/m, as well as the predictions isolating the contributions of the electron hopping (EH) and conductive networking (CN) mechanisms, are also depicted. It is observed that the present micromechanics approach provides very close agreements with the experimental data for filler volume fractions above the percolation threshold. In contrast, the experimental results reported very limited increases in the electrical conductivity for filler volume fractions below this critical concentration. In this case, the theoretical estimates only considering the conductive networking mechanism yield very close agreements. This is a fact that evidences the presence of some insulating effect on the filler interphases. Similar results were observed for CNT-reinforced cement-based materials [67], where the addition of chemical dispersants even partially insulates the matrix material. It is also observed in this figure that, once the filler content is higher than the percolation threshold, the conductive networking mechanism dominates the overall conductivity.
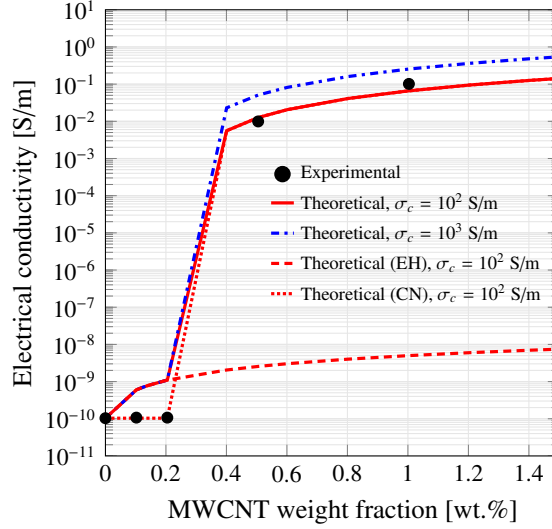
Figure 8: Overall electrical conductivity of MWCNT/epoxy composites (the experimental results have been taken from reference [22]).

4.1.2. Elastic properties of CNT/polymer composites

In this subsection, the previously fitted micromechanical variables are incorporated into the micromechanics modelling of the mechanical properties of MWCNT/epoxy composites. In this case, the experimental results reported by Vahedi *et al.* [66] are used as validation basis. The Young's modulus and Poisson's ratio of the epoxy matrix is selected as E_m=2.5 GPa and v_m=0.28, respectively. With regard to the elastic modulus of MWCNTs, experimental results for MWCNT modulus vary from 270 to 959 GPa [71]. For simplicity, a Young's modulus of 700 GPa is selected and MWCNTs are considered as isotropic solid rod-like inclusions. Fig. 9 investigates the effect of the interphase elastic modulus E_i with constant interphase thickness of t=20 nm. As expected, it is observed that the particle stiffening efficiency dramatically increases with increases in the interphase stiffness. In the particular case of $E_i = E_m$, the model degenerates into the standard two-phase Mori-Tanaka model. It is noted that the latter approach overestimates the experimental results, especially for high filler contents. Thus, this fact evidences the existence of interphase regions with softer properties than the hosting matrix material. In this case, the interfacial characteristics are defined at the nano-scale by means of certain interatomic potentials between the inclusions and the surrounding matrix. The characterization of such interactions would require the use of computationally demanding atomistic-based simulations. For the sake of simplicity, the thickness t and elastic modulus E_i of the interphase regions have been estimated through a least squares non-linear regression of the proposed approach with respect to the experimental data. As a result, values of t=31 nm E_i=2.17 GPa have been obtained. It can be observed in Fig. 10 that the estimates of the present approach with fitted interphase parameters are in very close agreements with the experimental data, yielding maximum differences below 5%. The biggest discrepancies are found for low filler contents. A more sophisticated simulation would require the consideration of the hollow structure of the MWCNTs, as well as the nano-scale inter-wall interaction along with the matrix-CNT interaction. For the aim of this work, the proposed approach is considered accurate enough.
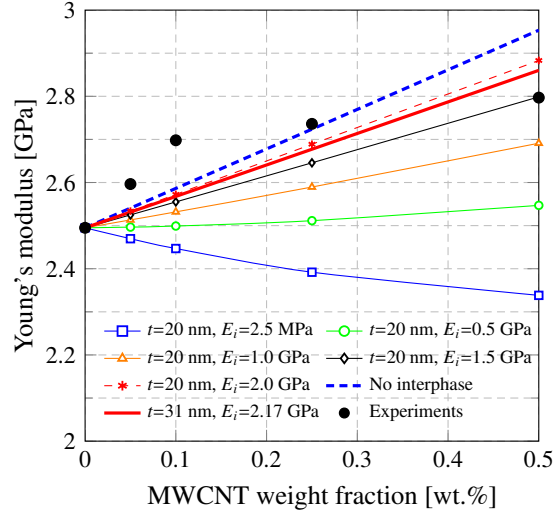
14

Figure 9: Prediction of the effective Young's modulus of MWCNT/epoxy composites with varying filler volume fraction and interphase properties. The experimental results have been taken from reference [66].
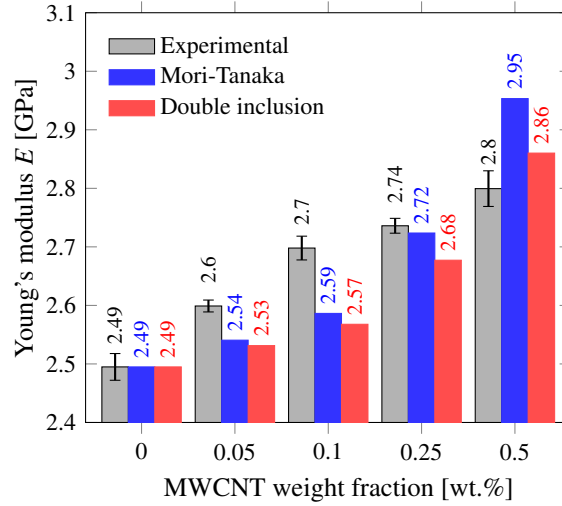

Figure 10: Comparison between the experimental effective Young's modulus and micromechanics approaches with and without interphase effects. The experimental results have been taken from reference [66], and the double inclusion approach has been computed considering t=31 nm and E_i=2.17 GPa.

Table 1: Fitted micromechanical variables of MWCNT/epoxy composites.

L_{cnt}	3.21 μm	E_{cnt}	700 GPa
D_{cnt}	10.35 nm	E_m	2.5 GPa
d_c	0.22 nm	ν_m	0.28
λ	0.69 eV	ν_{cnt}	0.3
σ_c	1.00E+02 S/m	t	31.00 nm
σ_m	1.04E-10 S/m	E_i	2.17 GPa
C_1	12.47	ρ_{cnt}	1.42 g/cm^3
C_2	1.02	ρ_m	1.12 g/cm^3

4.2. Post-buckling of CNT/polymer smart beams

In this section, detailed parametric analyses are presented to investigate the potential application of the proposed smart beams for buckling detection. Additionally, the numerical results are aimed at investigating the effect of the micromechanical parameters underlying the electromechanical behaviour of the sensing strips on the post-buckling response of the proposed smart beams. The geometrical dimensions of the smart beams are chosen as

15

1 m long and varying slenderness ratios L/h, namely L/h=20, 30 and 40. The MWCNT/epoxy strips are defined with a thickness of h_s=5 mm and are deployed on the top and bottom faces of host pristine epoxy beams. Additionally, two electrodes with a length L_e=5 cm are mounted on the external surfaces of the sensing strips with a separation from the supports of d_e=1 cm. A differential potential of 10 V is applied to the sensing strips, and the shunt resistors are defined with an electrical resistance of 100 Ω. For the sake of simplicity and generality, the following non-dimensional parameters are defined:

$$\overline{P} = P\frac{12L^2}{E_m B h^3} \tag{33}$$

$$\overline{w} = \frac{w}{h} \tag{34}$$

$$\overline{u} = \frac{u}{L} \tag{35}$$

where w and u stand for the mid-span transverse displacement and the end-shortening, respectively. Finally, in order to evaluate the imperfection sensitivity of the beams, two initial imperfection values, A_o, are defined as $A_o = h_n/1000$ and $A_o = h_n/10$ for perfect and imperfect beams, respectively.

4.2.1. Effective electromechanical properties of MWCNT/epoxy composites

The piezoresistivity coefficients have been computed under virtual experiments of laterally constrained uniaxial dilation and distortion as illustrated in Subsection 3.4. The resulting electromechanical parameters are collected in Table 2 and consider the micromechanical properties previously indicated in Table 1. Filler mass fractions ranging from 0.50% to 1.00% have been selected with steps of 0.10%. It is important to recall that CNT-based sensors exhibit a highly linear behaviour for such volume fractions, a fact that guarantees the accuracy of the used micromechanics approach. In Table 2, the piezoresistivity coefficients have been indicated both for compression (λ^-) and stretching (λ^+). It has been extensively reported in the literature [45] that CNT-reinforced composites exhibit different strain-sensitivities when subjected to compression or tensile efforts. However, the difference between the piezoresistivity coefficients under compression and traction is small enough that a common strain sensitivity is assumed, in this case the piezoresistivity coefficients under tension have been selected in the simulations for consistency with the experimental data.

Table 2: Effective electromechanical properties of MWCNT/epoxy composites.

	0.50 wt.%	0.60 wt.%	0.70 wt.%	0.80 wt.%	0.90 wt.%	1.00 wt.%
λ_{11}^+	6.84	5.68	4.85	4.21	3.68	3.23
λ_{12}^+	7.99	6.83	6.01	5.36	4.83	4.38
λ_{11}^-	7.37	6.12	5.24	4.54	3.97	3.48
λ_{12}^-	8.62	7.37	6.48	5.78	5.21	4.73
λ_{44}	1.19	1.19	1.19	1.19	1.19	1.19
σ [S/m]	1.22E-02	2.05E-02	3.01E-02	4.08E-02	5.27E-02	6.56E-02
E [Gpa]	2.86	2.93	3.01	3.08	3.15	3.23
ν	0.28	0.27	0.27	0.27	0.27	0.27

4.2.2. Parametric analyses and discussion

Fig. 11 investigates the influence of the MWCNT content on the post-buckling behaviour of the smart beams with slenderness ratio $L/h = 20$ considering H-H and C-C boundary conditions. In this figure, solid and dashed lines denote the results for perfect ($A_o = h_n/1000$) and imperfect ($A_o = h_n/10$) smart beams, respectively. It is first noted that, as expected, the post-buckling load-deflection curves of both perfect and imperfect smart beams rise with an increase in the MWCNT volume fraction. For instance, smart strips doped with 0.5 wt.% and 0.6% increase the critical buckling load of a H-H pristine epoxy beam with the same dimensions by around 9 and 10%, respectively. These results highlight the first benefit of the proposed smart strips which, besides conferring self-diagnostic properties, also behave as mechanical reinforcements. As expected, it is also noted that the buckling loads of C-C smart beams are considerably higher than those of H-H beams. Moreover, as it is well-known from structural stability theory, transverse displacements start at the critical buckling loads for ideal (perfect) smart beams, while imperfect beams exhibit no critical buckling load and their initial configuration enables the appearance of transverse displacements within the whole range of considered compressive loads. Such differences get progressively reduced in the post-buckling regime until the equilibrium paths of imperfect beams converge to those of ideal beams. In order to further this analysis, Fig. 12 depicts the non-dimensional compressive loads $\overline{P}$ versus the non-dimensional end-shortening $\overline{u}$ for smart beams considering different slenderness ratios, namely L/h=20, 30 and 40. It can be observed that higher slenderness ratios yield increasing critical buckling loads.
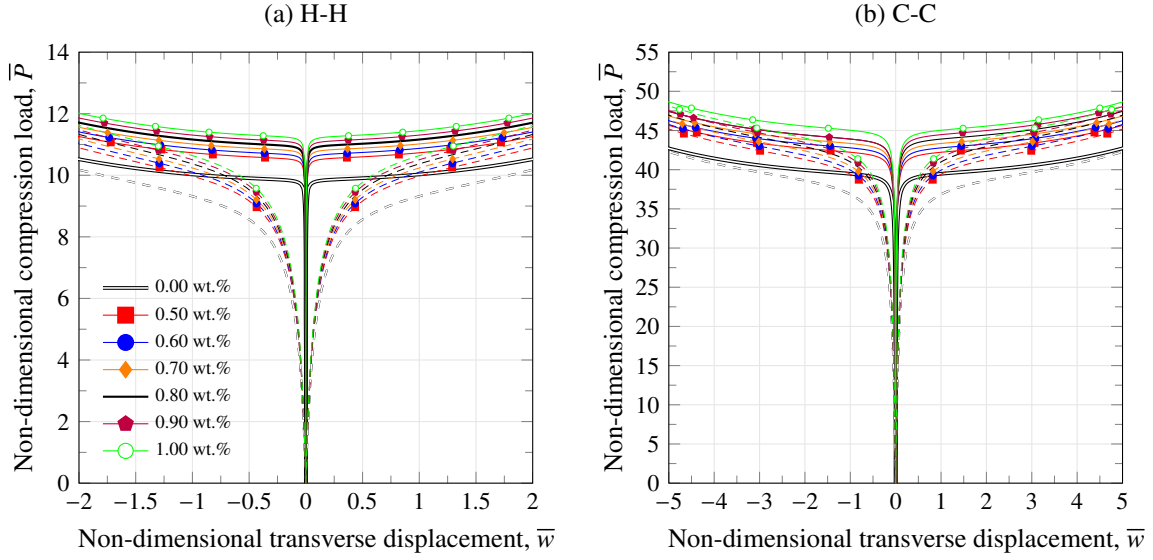
16

Figure 11: Compressive post-buckling equilibrium paths for smart beams with different MWCNT volume fractions for H-H (a) and C-C (b) boundary conditions. Solid and dashed lines denote the results for imperfect ($A_o = h_n/10$) and perfect ($A_o = h_n/1000$) smart beams, respectively. ($L/h = 20$).
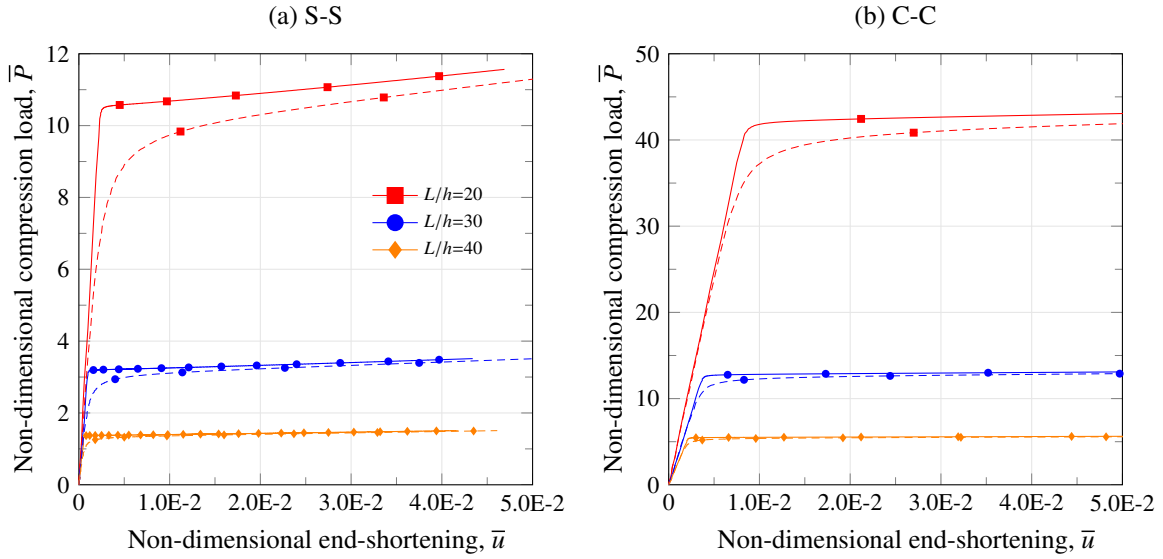

Figure 12: Non-dimensional compressive load versus non-dimensional end-shortening for imperfect ($A_o = h_n/10$) smart beams with different slenderness ratios L/h, and H-H (a) and C-C (b) boundary conditions (0.5 wt.%). The adimensionalization have been conducted considering the geometrical dimensions of smart beams with slenderness ratio $L/h = 20$ in all the cases for consistency purposes.

In the remainder of this section, the post-buckling behaviour of the proposed smart beams is investigated in terms of their electrical output. Fig. 13 depicts the electric current per unit of width flowing through the sensing strips versus the applied compressive load for H-H smart beams doped with varying MWCNT contents. In this figure, the results computed for both the top and bottom sensing strips are furnished with single and double lines, respectively. Firstly, it is observed that sensing strips doped with higher MWCNT concentrations output higher electric currents. This evidences that increasing MWCNT contents decrease the overall electrical resistance of the smart strips or, alternatively, increase the electrical conductivity of the composites as previously reported in Table 2. Comparing the electric currents outputted by the top and bottom strips, it is noted that both overlap until a certain point at which they suddenly diverge, that is, the critical buckling load $\overline{P}_{cr}$ of the beams. Considering that the beams buckle with positive transverse displacements in the y-axis direction (see Fig. 1), the buckling-induced bending efforts increase the compressive strains in the bottom strip while transfer tensile strains to the top strip. In this light, it is observed that the bottom strips furnish increasing electric currents after the buckling failure,

17

unlike the top strips. This indicates that the electrical resistance of the bottom strips decreases as a result of the bending-induced increasing compressive strains, and vice versa for the top strips. With regard to the imperfection sensitivity of the proposed smart beams, it is shown that imperfections accelerate the divergence of the electrical outputs provided by the top and bottom strips. Although a clear buckling point cannot be readily identified in this case, the electrical response of the sensors follows a similar behaviour and a region of potential buckling failure can be stated. Overall, it is concluded from these analyses that the proposed smart beams can be used for buckling detection through the monitoring of the buckling-induced non-linear electrical response of the sensing strips.
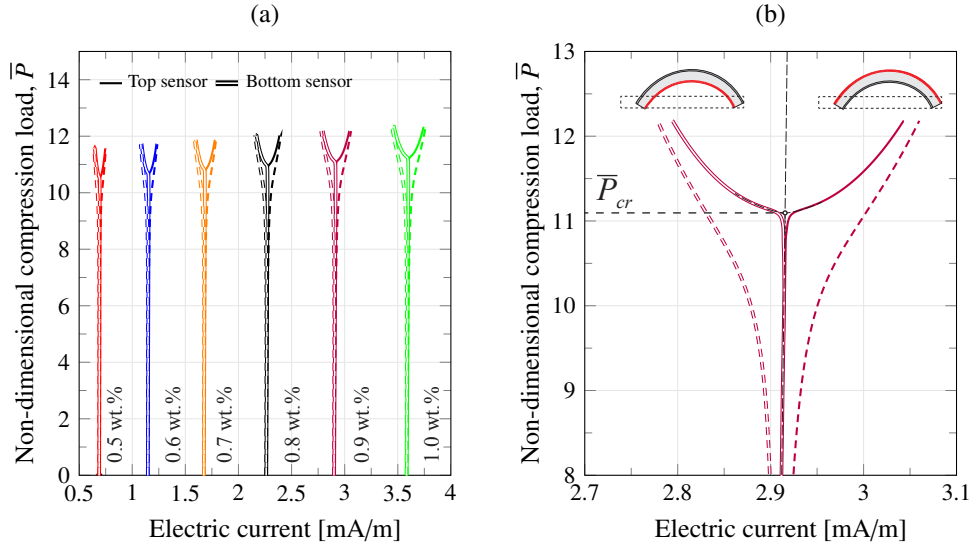

Figure 13: Non-dimensional compression load $\overline{P}$ versus electrical current per unit of width outputted by the strip-like strain sensors for varying filler contents (a), and detail view of the case of 0.9 wt.% MWCNTs (b). Solid and dashed lines denote the results for imperfect ($A_o = h_n/10$) and perfect ($A_o = h_n/1000$) smart beams, respectively. (L/h=20, S-S, L_e=5 cm, d_e=1 cm).

In order to further the previous analysis, Fig. 14 (a) and (b) depict the non-dimensional compression load $\overline{P}$ versus the relative variation of electrical resistance $\Delta R/R_o$ of the sensing strips with slenderness ratio L/h=30 deployed on H-H and C-C smart beams, respectively. It is noted that, in all cases, $\Delta R/R_o$ varies linearly with compression until the critical buckling load, where the output of the sensors becomes highly non-linear. The first linear part corresponds to the end-shortening of the beams prior to buckling. In the case of ideal smart beams ($A_o = h_n/10$), the slope of the linear part of the curves corresponds to the longitudinal piezoresistivity coefficient λ_{11}. Indeed, it is observed that the slopes for increasing MWCNT concentrations also increase in accordance with the piezoresistivity coefficients previously reported in Table 2. Once the smart beams buckle, the variation of the electrical resistances of the top and bottom strips exhibit opposite behaviours. In accordance with the results previously shown in Fig. 13, the top smart strips deployed on H-H beams experience increasing bending-induced tensile strains when buckling develops in the positive y-axis. It is noted that, as the buckling progresses, the bending efforts become dominant and the electrical resistance of the top strips increases above that of the unstrained system ($\Delta R/R_o$=0). Conversely, bending induces higher compressions in the bottom strips which accelerate the decrease of their electrical resistance initiated in the pre-buckling stage. In the case of C-C smart beams, a similar behaviour can be observed. Nevertheless, it is noticeable that, although the beams buckle at considerably higher critical loads compared with the former case, the relative variation of electrical resistance of the sensing strips after buckling takes similar values or even lesser than those in the case of H-H beams. The reason for these sensitivity values lies in the buckling mode of C-C beams and the specific electrodes layout as shown hereafter.

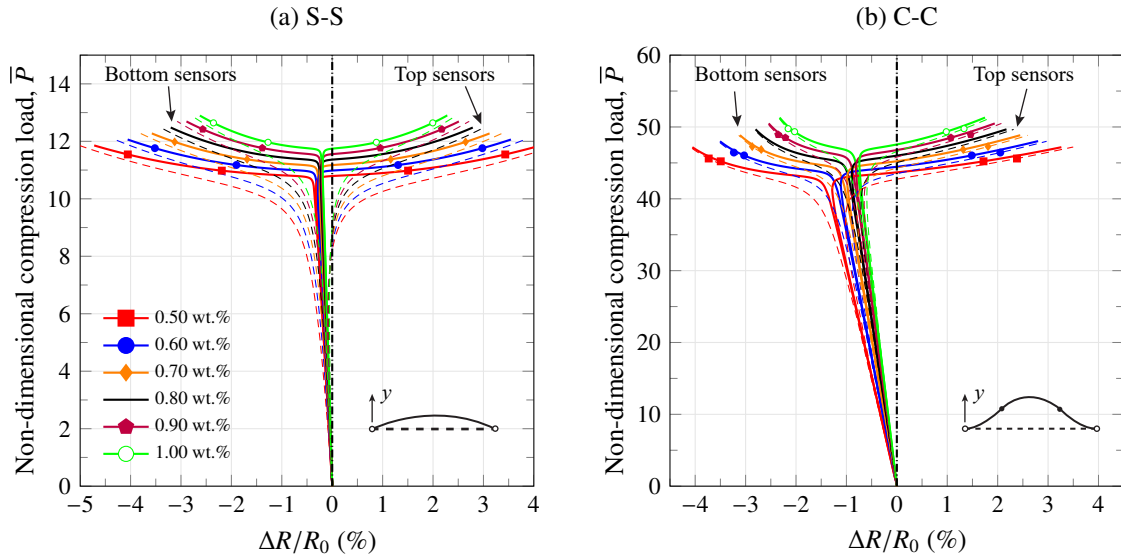Figure 14: Non-dimensional compression load $\overline{P}$ versus relative variation of electrical resistance $\Delta R/R_o$ of smart beams doped with different MWCNT contents and S-S (a) and C-C (b) boundary conditions. (L/h=30, L_e=5 cm, d_e=1 cm).

The proposed sensing strips for buckling detection relate the non-linear post-buckling behaviour of the smart beams to the variation of their electrical resistance between the electrodes. It is well-known that the buckling mode of fully clamped beams exhibits two inflection points located $L/4$ from each end. In this way, when the smart beams bow, the bending moment diagram has different signs at the ends and the mid-span. Therefore, the bending-induced variations in the electrical resistance of the sensing strips behave accordingly. In particular, given that rotations are constrained at the ends of the C-C beams, the overall variation of electrical resistance in the sensing strips equals zero. Hence, in order to assess such buckling modes, it is necessary to properly locate the electrodes in such a way that the monitoring restricts to certain bending areas resulting in measurable variations in the electrical output of the sensors. In order to illustrate this, Fig. 15 investigates the influence of the length of the electrodes L_e and the distance from the ends d_e in the case of C-C smart beams. Firstly, Fig. 15 (a) furnishes the post-buckling equilibrium paths of smart beams with electrodes deployed 1 cm far from the ends and with different lengths, namely L_e=5 cm and 1 cm. It is noted that the smart beams with 1 cm long electrodes exhibit considerably lower sensitivity values after buckling failure. In this particular case, the left branch of the post-buckling path, that is, the variation of the electrical resistance of the top sensor, even exhibits a change of tendency shortly after the buckling failure. Further, Fig. 15 (b) investigates the effect of the distance of the electrodes from the ends d_e while keeping the electrodes' length L_e=5 cm as a constant. It is noted that, in the case of d_e=20 cm, the sensitivity of the sensing strips substantially increases after the buckling failure. In this case, the sensing strips mostly capture the bending-induced normal strains of the central part of the buckled beam, what results in a clearer buckling detection. In this light, the ideal case of point electrodes located at the ends of the beam would exhibit no buckling sensitivity (a constant value of $\Delta R/R_o$ in the post-buckling regime), while point electrodes located at the inflection points would yield maximum sensitivities.
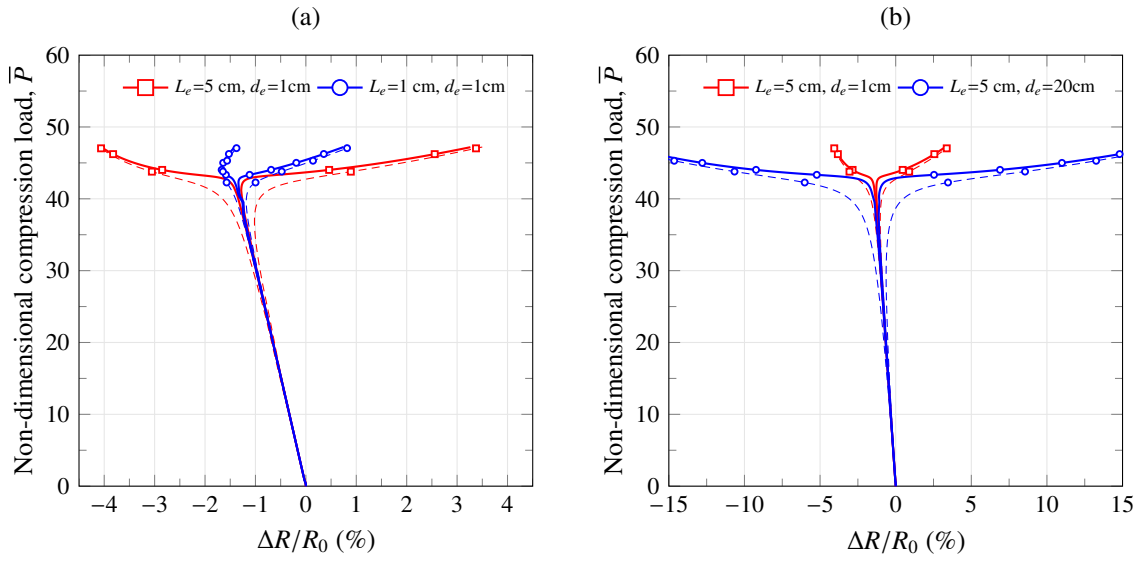
19

Figure 15: Non-dimensional compression load $\overline{P}$ versus relative variation of electrical resistance $\Delta R/R_o$ of C-C smart beams considering different electrodes' lengths L_e (a) and distances from the ends d_e (b). Solid and dashed lines denote the results for imperfect ($A_o = h_n/10$) and perfect ($A_o = h_n/1000$) smart beams, respectively (L/h=30, 0.5 wt.%).

5. Conclusions

In this paper, self-diagnostic smart beams has been proposed for buckling detection applications. This consists of MWCNT/epoxy strip-like sensors deployed on the upper and bottom faces of host pristine beams. Moreover, in order to relate the bending-induced normal strains following the buckling failure, a two-probe resistivity measurement scheme has been proposed. The theoretical estimates of the electromechanical constitutive properties of CNT-based composites have been benchmarked against experimental results from the literature, and good agreements have been reported in the determination of the elastic moduli, electrical conductivity and piezoresistivity coefficients. Afterwards, detailed parametric analyses have been presented to investigate the electrical response of the proposed beams under buckling failure, as well as to investigate the influence of the filler content, boundary conditions, and electrodes layout. The presented numerical results have demonstrated the effectiveness of the proposed smart beams for buckling detection, reporting measurable disturbances in their electrical output as a consequence of buckling failure. On the whole, the key findings of this work can be summarized as follows:

- The present micromechanics-based piezoresistivity model for CNT-based composites has been shown suitable for filler contents not too proximate to the percolation threshold. Around this critical filler load, the strain sensitivity of the composites exhibits a highly non-linear behaviour that fails to be accurately captured by the present approach. Nevertheless, composites doped with CNT contents slightly above the percolation threshold (as typically defined for CNT-based composites for SHM applications) exhibit a linear response to mechanical strains that can be accurately simulated by the present approach.

- The benefits of the proposed smart beams have been shown to be twofold: the MWCNT/epoxy strips act as mechanical reinforcements rising the critical buckling loads of the host beam and, simultaneously, they confer self-diagnostic abilities to the structural system.

- The presented parametric analyses have reported that the proposed smart beams exhibit noticeable disturbances in their electrical output when the buckling failure occurs. Moreover, symmetrically deployed MWCNT/epoxy strips have been shown effective to isolate the maximum bending-induced changes in the longitudinal strains.

- The numerical results have showed that a clear divergence between the electrical outputs of the top and bottom sensing strips are observed when perfect smart structures buckle. Nonetheless, when geometric imperfections are included, there is not a clear divergence point but a divergence region.

- The electrodes layout has been demonstrated to represent a key aspect in the design of the proposed smart beams. In particular, numerical results and discussion have been provided on the influence of the length and position of the electrodes on the buckling detection capacities. It has been concluded that for beam-like structures that bow following buckling modes with inflection points, it is paramount to tailor the position of the electrodes in order to isolate bending regions with constant sign.

References

[1] P. C. Chang, A. Flatau, S. C. Liu, Health monitoring of civil infrastructure, Structural health monitoring 2 (2003) 257–267.

[2] S. Das, P. Saha, S. K. Patro, Vibration-based damage detection techniques used for health monitoring of structures: a review, Journal of Civil Structural Health Monitoring 6 (2016) 477–507.

[3] A. D. B. Ferreira, P. R. Nóvoa, A. T. Marques, Multifunctional material systems: A state-of-the-art review, Composite Structures (2016).

[4] M. Rafiee, F. Nitzsche, M. Labrosse, Dynamics, vibration and control of rotating composite beams and blades: A critical review, Thin-Walled Structures 119 (2017) 795–819.

[5] J. Singer, J. Arbocz, T. Weller, Buckling experiments: experimental methods in buckling of thin-walled structures. Shells, built-up structures, composites and additional topics, Wiley Online Library, 2002.

21

[6]   F. J. Shaker, Effect of axial load on mode shapes and frequencies of beams (1975).

[7]   R. H. Plaut, L. N. Virgin, Use of frequency data to predict buckling, Journal of Engineering Mechanics 116 (1990) 2330–2335.

[8]   H. Abramovich, D. Govich, A. Grunwald, Buckling prediction of panels using the vibration correlation technique, Progress in Aerospace Sciences 78 (2015) 62–73.

[9]   W. Qu, W. Song, Y. Xia, Y. Xu, W. Qin, Z. Jiang, Two-step method for instability damage detection in tower body of transmission structures, Advances in structural engineering 16 (2013) 219–232.

[10] G. Yan, C. Fang, R. Feng, X. Hua, Y. Zhao, Detection of member overall buckling in civil space grid structures based on deviation in normal strain along the member, Engineering Structures 131 (2017) 599–613.

[11] J. W. Park, C. Y. Ryu, H. K. Kang, C. S. Hong, Detection of buckling and crack growth in the delaminated composites using fiber optic sensor, Journal of Composite Materials 34 (2000) 1602–1623.

[12] F. Ravet, L. Zou, X. Bao, L. Chen, R. F. Huang, H. A. Khoo, Detection of buckling in steel pipeline and column by the distributed Brillouin sensor, Optical Fiber Technology 12 (2006) 305–311.

[13] X. Feng, W. Wu, X. Li, X. Zhang, J. Zhou, Experimental investigations on detecting lateral buckling for subsea pipelines with distributed fiber optic sensors, Smart Structures and Systems 15 (2015) 245–258.

[14] C. Y. Ryu, J. R. Lee, C. G. Kim, C. S. Hong, Buckling behavior monitoring of a composite wing box using multiplexed and multi-channeled built-in fiber Bragg grating strain sensors, NDT & E International 41 (2008) 534–543.

[15] A. Alaimo, A. Milazzo, C. Orlando, Numerical analysis of a piezoelectric structural health monitoring system for composite flange-skin delamination detection, Composite Structures 100 (2013) 343–355.

[16] D. Pieper, K. M. Donnell, O. Abdelkarim, M. A. ElGawady, Embedded FSS sensing for structural health monitoring of bridge columns, IEEE, 2016, pp. 1–5.

[17] J. Vigui, P. J. J. Dumont, Analytical post-buckling model of corrugated board panels using digital image correlation measurements, Composite Structures 101 (2013) 243–254.

[18] C. Li, E. T. Thostenson, T. W. Chou, Sensors and actuators based on carbon nanotubes and their composites: a review, Composites Science and Technology 68 (2008) 1227–1249.

[19] C. González, J. J. Vilatela, J. M. Molina-Aldareguía, C. S. Lopes, J. LLorca, Structural composites for multifunctional applications: current challenges and future trends, Progress in Materials Science 89 (2017) 194–251.

[20] H. S. Shen, Y. Xiang, Postbuckling of functionally graded graphene-reinforced composite laminated cylindrical shells subjected to external pressure in thermal environments, Thin-Walled Structures 124 (2018) 151–160.

[21] D. G. Ninh, Nonlinear thermal torsional post-buckling of carbon nanotube-reinforced composite cylindrical shell with piezoelectric actuator layers surrounded by elastic medium, Thin-Walled Structures 123 (2018) 528–538.

[22] R. Pilawka, S. Paszkiewicz, Z. Rosłaniec, Epoxy composites with carbon nanotubes, Advances in Manufacturing Science and Technology 36 (2012) 67–79.

[23] A. Sanli, C. Müller, O. Kanoun, C. Elibol, M. F. X. Wagner, Piezoresistive characterization of multi-walled carbon nanotube-epoxy based flexible strain sensitive films by impedance spectroscopy, Composites Science and Technology 122 (2016) 18–26.

[24] R. Howser, H. Dhonde, Y. Mo, Self-sensing of carbon nanofiber concrete columns subjected to reversed cyclic loading, Smart Materials and Structures (2011).

[25] A. Meoni, A. D'Alessandro, A. Downey, E. García-Macías, M. Rallini, A. L. Materazzi, L. Torre, S. Laflamme, R. Castro-Triguero, F. Ubertini, An experimental study on static and dynamic strain sensitivity of embeddable smart concrete sensors doped with carbon nanotubes for shm of large structures, Sensors 18 (2018) 831.

[26] T. Schumacher, E. T. Thostenson, Development of structural carbon nanotube–based sensing composites for concrete structures, Journal of Intelligent Material Systems and Structures 25(11) (2013) 1331–1339.

[27] A. D'Alessandro, M. Rallini, F. Ubertini, A. L. Materazzi, J. M. Kenny, Investigations on scalable fabrication procedures for self-sensing carbon nanotube cement-matrix composites for SHM applications, Cement and Concrete Composites 65 (2016) 200–213.

[28] F. Naeem, H. K. Lee, H. K. Kim, I. W. Nam, Flexural stress and crack sensing capabilities of MWNT/cement composites, Composite Structures 175 (2017) 86–100.

[29] A. Downey, A. D'Alessandro, S. Laflamme, F. Ubertini, Smart bricks for strain sensing and crack detection in masonry structures, Smart Materials and Structures 27 (2017) 015009.

[30] I. Kang, M. J. Schulz, J. H. Kim, V. Shanov, D. Shi, A carbon nanotube strain sensor for structural health monitoring, Smart Materials and Structures 15 (2006) 737–748.

[31] A. V. Desai, M. A. Haque, Mechanics of the interface for carbon nanotube-polymer composites, Thin-Walled Structures 43 (2005) 1787–1803.

[32] R. Rafiee, R. M. Moghadam, On the modeling of carbon nanotubes: A critical review, Composites Part B: Engineering 56 (2014) 435–449.

[33] R. Zhu, E. Pan, A. K. Roy, Molecular dynamics study of the stress–strain behavior of carbon-nanotube reinforced Epon 862 composites, Materials Science and Engineering: A 447 (2007) 51–57.

[34] A. K. Gupta, S. P. Harsha, Analysis of mechanical properties of carbon nanotube reinforced polymer composites using multi-scale finite element modeling approach, Composites Part B: Engineering 95 (2016) 172–178.

[35] M. Rouhi, M. Rais-Rohani, Modeling and probabilistic design optimization of a nanofiber-enhanced composite cylinder for buckling, Composite Structures 95 (2013) 346–353.

[36] W. Xu, F. Wu, Y. Jiao, M. Liu, A general micromechanical framework of effective moduli for the design of nonspherical nano-and micro-particle reinforced composites with interface properties, Materials & Design 127 (2017) 162–172.

[37] E. García-Macías, R. Castro-Triguero, F. Ubertini, Two-step hierarchical micromechanics model of partially saturated porous composites doped with ellipsoidal particles with interface effects, Composites Part B: Engineering 148 (2018) 49–60.

[38] C. Feng, L. Jiang, Investigation of uniaxial stretching effects on the electrical conductivity of CNT-polymer nanocomposites, Journal of Physics D: Applied Physics 47 (2014) 405103.

[39] L. Chang, K. Friedrich, L. Ye, P. Toro, Evaluation and visualization of the percolating networks in multi-wall carbon nanotube/epoxy composites, Journal of materials science 44 (2009) 4003–4012.

[40] F. Deng, Q. S. Zheng, An analytical model of effective electrical conductivity of carbon nanotube composites, Applied Physics Letters 92 (2008) 071902.

[41] T. Takeda, Y. Shindo, Y. Kuronuma, F. Narita, Modeling and characterization of the electrical conductivity of carbon nanotube-based polymer composites, Polymer 52 (2011) 3852–3856.

[42] C. Feng, L. Jiang, Micromechanics modeling of the electrical conductivity of carbon nanotube (CNT)–polymer nanocomposites, Composites Part A: Applied Science and Manufacturing 47 (2013) 143–149.

[43] N. Hu, H. Fukunaga, S. Atobe, Y. Liu, J. Li, Piezoresistive strain sensors made from carbon nanotubes based polymer nanocomposites, Sensors 11 (2011) 10691–10723.

[44] T. Tallman, K. Wang, An arbitrary strains carbon nanotube composite piezoresistivity model for finite element integration, Applied Physics Letters 102 (2013) 011909.

[45] E. García-Macías, A. D'Alessandro, R. Castro-Triguero, D. Pérez-Mira, F. Ubertini, Micromechanics modeling of the uniaxial strain-sensing property of carbon nanotube cement-matrix composites for SHM applications, Composite Structures 163 (2017) 195–215.

[46] L. Y. Alamusi, N. Hu, Numerical simulations on piezoresistivity of CNT/polymer based nanocomposites, Computers Materials & Continua 20 (2010) 101–117.

[47] C. Feng, L. Jiang, Micromechanics modeling of bi-axial stretching effects on the electrical conductivity of CNT-polymer composites, International Journal of Applied Mechanics 7 (2015) 1550005.

[48] E. García-Macías, R. Castro-Triguero, A. Sáez, F. Ubertini, 3D mixed micromechanics-FEM modeling of piezoresistive carbon nanotube smart concrete, Computer Methods in Applied Mechanics and Engineering 340 (2018) 396–423.

[49] W. K. Hsu, V. Kotzeva, P. C. P. Watts, G. Z. Chen, Circuit elements in carbon nanotube-polymer composites, Carbon 42 (2004) 1707–1712.

[50] A. Alizadeh Sahraei, M. Ayati, M. Baniassadi, D. Rodrigue, M. Baghani, Y. Abdi, AC and DC electrical behavior of MWCNT/epoxy nanocomposite near percolation threshold: Equivalent circuits and percolation limits, Journal of Applied Physics 123 (2018) 105109.

[51] A. Downey, A. D'Alessandro, F. Ubertini, S. Laflamme, R. Geiger, Biphasic DC measurement approach for enhanced measurement stability and multi-channel sampling of self-sensing multi-functional structural materials doped with carbon-based additives, Smart Materials and Structures 26 (2017) 065008.

[52] A. Downey, A. DAlessandro, M. Baquera, E. García-Macías, D. Rolfes, F. Ubertini, S. Laflamme, R. Castro-Triguero, Damage detection, localization and quantification in conductive smart concrete structures using a resistor mesh model, Engineering Structures 148 (2017) 924–935.

[53] M. Hori, S. Nemat-Nasser, Double-inclusion model and overall moduli of multi-phase composites, Mechanics of Materials 14 (1993) 189–206.

[54] W. Xu, H. Ma, S. Ji, H. Chen, Analytical effective elastic properties of particulate composites with soft interfaces around anisotropic particles, Composites Science and Technology 129 (2016) 10–18.

[55] J. K. Beddow, Particle Characterization in Technology: Volume II: Morphological Analysis, CRC press, 2018.

[56] J. G. Simmons, Generalized formula for the electric tunnel effect between similar electrodes separated by a thin insulating film, Journal of Applied Physics 34 (1963) 1793–1803.

[57] G. D. Seidel, D. C. Lagoudas, A micromechanics model for the electrical conductivity of nanotube-polymer nanocomposites, Journal of Composite Materials 43 (2009) 917–941.

[58] K. Yan, Q. Xue, Q. Zheng, L. Hao, The interface effect of the effective electrical conductivity of carbon nanotube composites, Nanotechnology 18 (2007) 255705.

[59] G. M. Odegard, T. S. Gates, Constitutive modeling of nanotube/polymer composites with various nanotube orientation, in: 2002 SEM Annual Conference on Experimental and Applied Mechanincs.

[60] M. Taya, Electronic composites: modeling, characterization, processing, and MEMS applications, Cambridge University Press, 2005.

[61] T. Komori, K. Makishima, Numbers of fiber-to-fiber contacts in general fiber assemblies, Textile Research Journal 47 (1977) 13–17.

[62] V. Kumar, A. Rawal, Tuning the electrical percolation threshold of polymer nanocomposites with rod-like nanofillers, Polymer 97 (2016) 295–299.

[63] A. Sobha, S. K. Narayanankutty, Improved strain sensing property of functionalised multiwalled carbon nanotube/polyaniline composites in TPU matrix, Sensors and Actuators A: Physical 233 (2015) 98–107.

[64] G. K. Johns, Modeling piezoresistivity in silicon and polysilicon, Journal of Applied Engineering Mathematics April 2 (2006) 1–5.

[65] Structural analysis guide, Release 15.0, ANSYS Inc, Cannonsburg, PA (2014).

[66] F. Vahedi, H. R. Shahverdi, M. M. Shokrieh, M. Esmkhani, Effects of carbon nanotube content on the mechanical and electrical properties of epoxy-based composites, New Carbon Materials 29 (2014) 419–425.

[67] E. García-Macías, A. D'Alessandro, R. Castro-Triguero, D. Pérez-Mira, F. Ubertini, Micromechanics modeling of the electrical conductivity of carbon nanotube cement-matrix composites, Composites Part B: Engineering 108 (2017) 451–469.

[68] C. Laurent, E. Flahaut, A. Peigney, The weight and density of carbon nanotubes versus the number of walls and diameter, Carbon 48 (2010) 2994–2996.

[69] M. M. Shokrieh, M. Esmkhani, Z. Shokrieh, Z. Zhao, Stiffness prediction of graphene nanoplatelet/epoxy nanocomposites by a combined molecular dynamics-micromechanics method, Computational Materials Science 92 (2014) 444–450.

[70] M. Park, H. Kim, J. P. Youngblood, Strain-dependent electrical resistance of multi-walled carbon nanotube/polymer composite films, Nanotechnology 19 (2008) 055705.

[71] M. F. Yu, O. Lourie, M. J. Dyer, K. Moloni, T. F. Kelly, R. S. Ruoff, Strength and breaking mechanism of multiwalled carbon nanotubes under tensile load, Science 287 (2000) 637–640.